MSc in Computational Physics

Carlos Rodríguez Molinuevo, zph330@alumni.ku.dk

Master's thesis

Transition from drift-wave to interchange turbulence in magnetically confined plasmas

Supervisor: Troels Haugbølle, haugboel@nbi.ku.dk

Supervisor: Anders Henry Nielsen, ahnie@fysik.dtu.dk

Co-Supervisor: Matthias Wiesenberger, mattwi@fysik.dtu.dk

Niels Bohr Institute Fag. July 30, 2021

Abstract

Throughout this work, we present a novel technique to characterize drift-wave and interchange turbulence in the limits of the last closed flux surface. This method is based on the study of the phase relation between electrostatic potential and density as well as between radial velocity and density using the cross power spectral density. 2D simulations, written using FELTOR, of an interchange and the modified Hasegawa-Wakatani models are studied. Using these simulations we are able to measure and provide the differences between drift-wave and interchange instability. When measuring the phase shift between potential and density, we get a 0 rad difference for drift-wave turbulence and $\frac{\pi}{2}$ rad for interchange. When comparing the phase difference between radial transport and density, the results are the opposite, 0 rad for interchange and $\frac{\pi}{2}$ rad for drift-wave. Afterwards, a complete model is proposed where plasma dynamic is studied in the regions around the last closed flux surface, the edge and the scrape-off layer. From these simulations we measure a mixture of interchange and drift-wave turbulence in the limits of the edge region, where the phase relation between radial velocity and density becomes $\frac{\pi}{4}$ rad. This allow us to measure the contribution of both instabilities when they co-exist. Furthermore, we find a change of regime when crossing the last closed flux surface, the phase relation drops to 0 rad at the last closed flux surface, which can be used to measure the position of it. Finally, this technique is applied to state-of-the-art experimental data from the EAST tokamak reactor, where different phase relations are measured at the edge and at the scrape-off layer. The phase relation between electron temperature and floating potential change from $-\pi$ rad in the edge to $-\frac{3\pi}{4}$ rad in the scrape-off layer. This result could be used to locate the last closed flux surface, reducing the cost of this process.

Contents

Chapter 1

Introduction

In recent years, nuclear fusion has become a main interest as an energy source. Specially in a world suffering from climate change, where the dependency towards fossil fuels, such as coal, petrol or gas; is still increasing. Fossil energy sources are not only harmful for the environment but a main cause of death in 2015 6.5 million deaths were linked just to air pollution [1]. Substituting highly emitting sources by low carbon footprint ones is one of the main strategies to combat anthropogenic climate change, as since industrialization CO_2 emissions have been increasing continuously. Nowadays, renewable energies and nuclear fission energy are the best tools to reduce the CO_2 emissions, as well as the emissions of other green house effect gasses [2]. Specially since current renewable energies need from other sources to maintain the continuity of the electric grid.

Furthermore, the increasing energy consumption will generate a shortage of the previously mention energy sources [3]. In the case of fossil fuels, we should run out of oil and natural gas in about 50 years, while we should have coal for another 100 years. The uranium used in nuclear fission should last for 80 years, indicated by the current known reservoirs. In the case of nuclear fission, the odds can change greatly, as more efficient reactors are been created, IV Generation, and new ways of extracting Uranium from seawater are been investigated [4]. The situation for renewable energies is also not ideal neither, as the materials for construction are also limited.

In such scenario, nuclear fusion is presented as a solution to the most important challenges of the future. Nuclear fusion is the inverse process of nuclear fission. Instead of breaking heavy atoms, as Uranium, into lighter atoms releasing energy, light atoms, as hydrogen or helium, are collided with the intention of generating heavier atoms and energy. For this reason, nuclear fusion has the advantages of nuclear fission energy, as it does not produce any greenhouse emission, and solves the disadvantages of it, as it does not generate highly radioactive nuclei.

Nuclear fusion aims to generate energy by using deuterium, D, and tritium, T, which are hydrogen isotopes with one and two neutrons respectively [5]. This reaction emits an alpha particle, α, which is a helium nuclei, and a neutron, n,

$$D + T \rightarrow \alpha + n + 17.6 \text{ MeV}. \tag{1.1}$$

In the further future, we expect to use D and helium-3, ^{3}He, which releases more energy and a proton, p, instead of a neutron,

$$D + {}^3\text{He} \rightarrow \alpha + p + 18.3 \text{ MeV}. \tag{1.2}$$

The most worrying generated particle from this reactions are the neutrons, which are expected to be absorbed by the walls of the reactor. For this reason, the walls inside the reactor, the blankets, are made of lithium, Li, which can be broken to breed T when it absorbs a neutron [5],

$$^6\text{Li} + n \rightarrow \alpha + T + 4.8 \text{ MeV}. \tag{1.3}$$

$$^7\text{Li} + n \rightarrow \alpha + T + n - 2.5 \text{ MeV}. \tag{1.4}$$
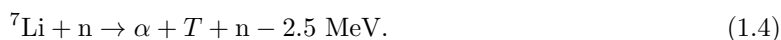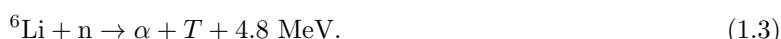
Currently, all the nuclear reactors work using only D, as we are still in the process of reaching stable nuclear fusion. The abundance of D is about 2 billion years, as it can be easily extracted from seawater. T is more difficult to obtain, as it is radioactive and it has a half-life of 12.2 years. Therefore, the only way of getting it is from ^{6}Li, from which we have enough supply for 20000 years [5].

For ^{3}He, we do not have any natural supply, it is produced by the β decay of T and it has only been generated as part of the nuclear weapons program [6]. Although it is abundant in the moon, which has reached there through solar wind [7].

Still, even if the use of nuclear fusion seems ideal, the complexity of nuclear fusion has become a headache for physicist. Nuclear fusion is the process that make stars shine and generate energy. Therefore, if we want to create efficient nuclear fusion reactions, we need to imitate the conditions inside a star, by heating the nuclear fuel until it reaches the state of plasma. Plasma is often called the fourth state of matter and at this state the atomic nuclei are completely separated from their electrons and move fast enough to fusion when colliding with other nuclei. As we cannot imitate the high pressure conditions inside stars, the plasma is heated to and much higher temperatures than the ones seems in stars, with much lower density.

Since the first attempt of making a nuclear fusion reactor in 1938, there is still no reactor capable of being self-sustainable. Which has ended up in the creation of several nuclear fusion type reactors [8], creating 2 big groups: inertial confinement and magnetic confinement. In inertial confinement reactors, lasers are used to heat up and compress a small pellet of fuel, such that it explodes generating fusion. In magnetic confinement, gas of nuclear fuel is heated up using electromagnetic fields, until it reaches temperatures of millions of Kelvins. At this temperature, the gas becomes plasma, an state where nuclei moves fast enough to fusion when colliding with other nuclei. An example of both kind of confinement can be seen in figure 1.1. Our study will be focused in this second group, magnetic confinement.
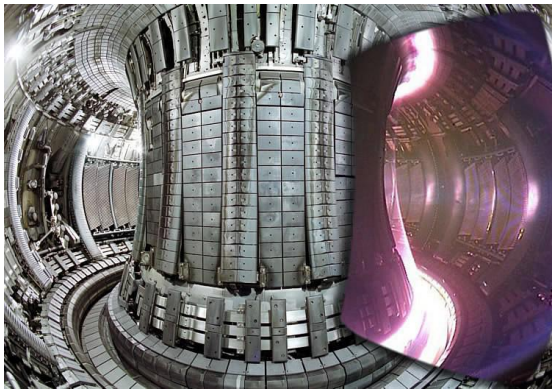
(a) From http://iter.org/, view inside of a magnetic confinement nuclear reactor with and without plasma.
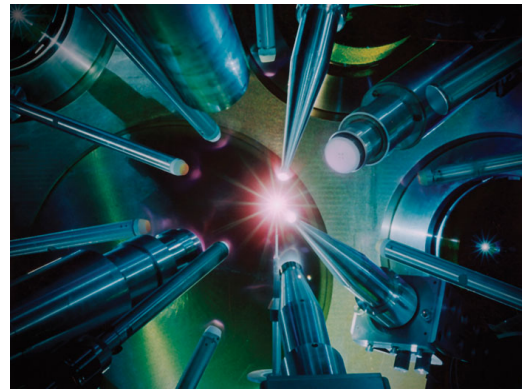

(b) Credit: Lawrence Livermore National Laboratory. Implosion of a fuel pellet creating similar conditions to sun inside an inertial confinement fusion reactor.

Figure 1.1: Illustrations of a magnetic confinement and inertial confinement nuclear fusion reactors.

1.1 Magnetic confinement

Magnetic confinement is nowadays the most promising nuclear fusion confinement. Although most of the magnetic confinement reactors use a torus shaped cavity for containing the plasma, 2 types stand out: the stellarators and the tokamaks. The first stellarator was developed in the United States in 1951 by Lyman Spitzer, Jr., and Martin Schwarzschild at Princeton University, this was the figure-8 shaped Model A-1, that can be seen in figure 1.2a. Tokamaks were developed in the USSR in 1951, by Igor Tamm and Andrei Sakharov, where the first working tokamak was created in 1958 by Natan Yavlinsky, this was the T-1, which can be seen in figure 1.2b. Nowadays, these reactors look quite similar from outside, we still can see how the cavity inside stellarators are twisted, as seen in figures 1.2c and 1.2d.

In both cases, a helical magnetic field is needed to control the plasma while heating it up. To avoid the charge separation due to the ∇B drift, we need to twist the magnetic field. By using this method, electrons, which follow the magnetic field lines, do not get trapped in one side of the reactor. In case they did, they would generate a large electric field and a big plasma transport that would end up hitting the walls and damaging the reactor. Here is where the main difference between them can be seen [9]. Tokamaks maintain themselves symmetricals, creating a toroidal magnetic field with
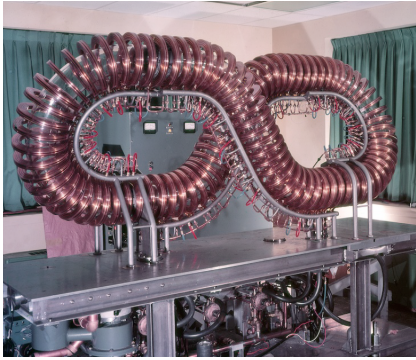
(a) From https://lynceans.org/, picture of one of the last figure-8 stellarators, built in 1958.
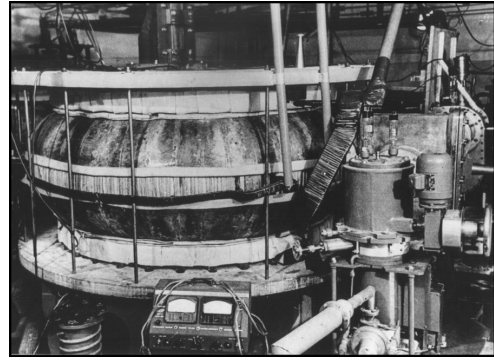
(b) From http://iter.org/, picture of the first tokamak reactor, T-1.
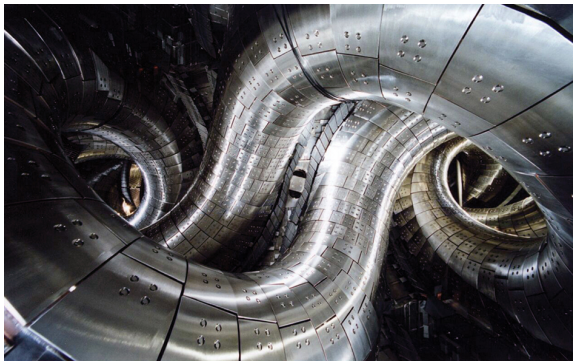
(c) From https://www-lhd.nifs.ac.jp/pub/LHD_Project_en.html, picture from the inside of the LHD stellarator, built in 1998 in Japan.

(d) From http://english.ipp.cas.cn/rh/east/, picture from the inside of the EAST tokamak reactor, built in 2006 in China.

Figure 1.2: Pictures of one of the first stellerator and tokamak reactors on top and from the currently in use reactors.

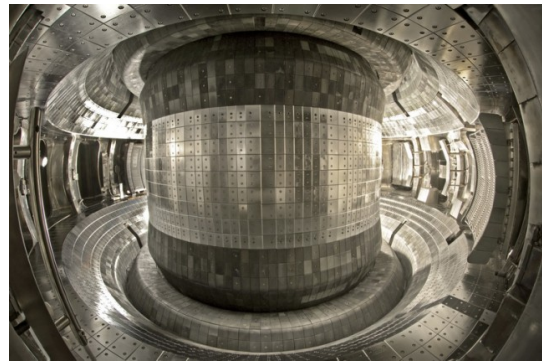the symmetrical coils that wrap the cavities. While a polidal magnetic field is created due to the plasma current, the same that heats the fuel, as seen in figure 1.3a. Stellarators in the other hand, are non-axisymetrical, with a structure that is used to twist the magnetic field, as illustrated in 1.3b. This makes tokamaks simpler to produce and more largely investigated, and the ones that will be studied in this work. Although our work can be extrapolated to a stellarator.

While the project ITER [10] expects to reach stable and self-sustainable nuclear fusion by 2035, with deuterium - tritium reactions, there is quite a lot of research that has to be done. Specially in the area of plasma dynamics inside tokamak reactors. During this work, we shall present a novel approach to characterize the turbulence in the region around the last closed flux surface (LCFS). The LCFS is the region where the magnetic field lines pass from being closed inside the reactor to cross the walls of it. This method will be capable of enlightening the path to stable and self-sustainable nuclear fusion. The LCFS also separates the inner or edge region, the center of the reactor where we expect to confine the plasma, where drift wave (DW) turbulence dominates; and the scrape-off layer (SOL), the region after the LCFS, where interchange (IC) turbulence dominates the dynamics. A scheme of this region is depicted in figure 1.4, where the edge or inner region refer to the are between closed magnetic surfaces and the separatrix. While during drift wave turbulence we get an in-efficient the transport of particles, interchange turbulence is a perfect transport mechanism. For this reason, it is important to be able of studying how and when they are present inside plasma dynamics. This approach will be done in 2D, due to its simplicity and time constrains. Further studies will need of a more complex model and to scale the system to 3D.
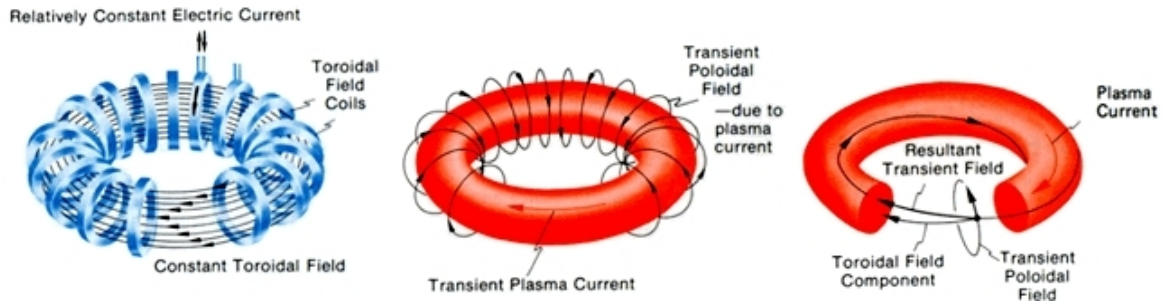
(a) From https://www.pppl.gov/, scheme of a Tokamak reactor and the magnetic field inside of it.
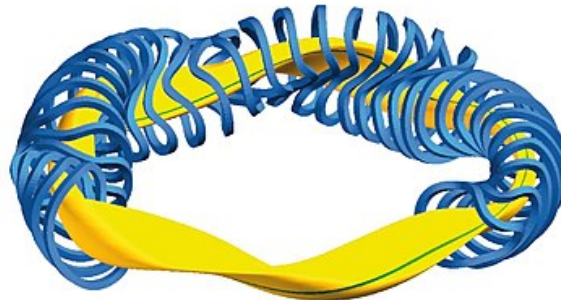
(b) From https://www.ipp.mpg.de/w7x Max-Planck Institut für Plasmaphysik, scheme of the Wendelstein 7-X stellerator in Germany.

Figure 1.3: Schemes of the Tokamak and Stellerator magnetic confinement nuclear reactors.
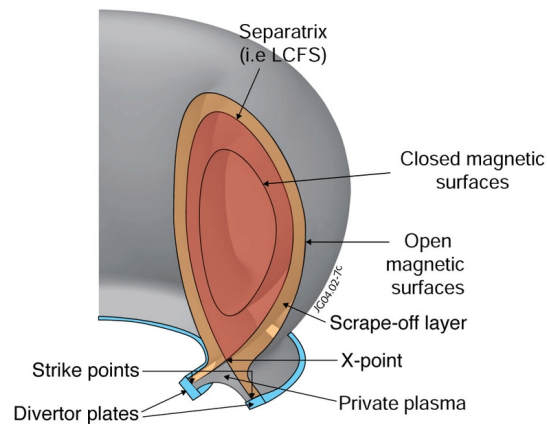

Figure 1.4: Source: EFDA-JET, sketch of the different regions inside a tokamak, based on the profile of the magnetic field.

Chapter 2

Theory

Before discussing in detail the project developed throughout the thesis, an explanation of the basic physics and mathematics must be done. For that propose, we need to explain the models used to approximate the physical domain inside a magnetic confinement reactor, of the Tokamak type. This is going to be done by explaining the collective motion of charged particles inside electromagnetic fields and by simplifying the main equations that describe the motion of plasma. Furthermore, we will explain the diagnostic done in EAST (the Experimental Advanced Superconducting Tokamak) tokamak reactor in Hefei [11], [12] and how can we use the data obtained from it.

2.1 Collective motion in a plasma, $\mathbf{v_{E \times B}}$, $\mathbf{v}_D$ and $\mathbf{v}_p$

As it has been explained, magnetic confinement reactors use magnetic fields to confine the plasma and control its dynamics. Therefore, it is important to generate a picture of the plasma's motion inside an electromagnetic field, where magnetic field will be generated by the coils surrounding the reactor and the electric field will be a consequence of the charged particles. For that, we shall start with the momentum conservation equation [13], where we introduce Lorentz force for charged fluid, due to the electromagnetic fields; and the pressure gradient, due to the fluid behaviour,

$$mn\frac{\mathrm{d}\mathbf{v}}{\mathrm{d}t} = qn(\mathbf{E} + \mathbf{v} \times \mathbf{B}) - \boldsymbol{\nabla}p, \tag{2.1}$$

where m is the mass of each particle, n is the density, $\mathbf{v}$ is the velocity, q is the charge of each particle, $\mathbf{E}$ is the electric field, $\mathbf{B}$ is the magnetic field and p is the pressure. As a comment, in the most general case, pressure is a tensor with an isotropic term filling the diagonal and an anisotropic term in the off-diagonal. The anisotropic term generates a first order dissipation term, that will be replaced by a hyperdiffusive term for numerical stability propose. For that reason, throughout the work, we will be only interested in the isotropic term, independent of the direction. Therefore, pressure will be taken as a scalar quantity.

The addition of forces to the system will generate drifts of the charged particles [5], [14]–[16]. For the current situation, there are three drifts of great interest, the $\mathbf{E} \times \mathbf{B}$, the diamagnetic and the polarization drifts. The first one is caused by the addition of an electric field, in our case, due to the ionization of the particles in the plasma. The second one is caused by a pressure gradient, caused by the gradient of density inside the torus, the reactor confines the fuel in the center of it, this generates a density reduction along the radial direction. The last one is caused due to a time variation of the electric field, particles will try to follow the electric field.

The $\mathbf{E} \times \mathbf{B}$ and diamagnetic drifts will be studied together as they can be easily extracted from equation 2.1. For the polarization drift, we need to add perturbation theory, which will be done separately.

2.1.1 $\mathbf{E} \times \mathbf{B}$ and diamagnetic drifts

To obtain the $\mathbf{E} \times \mathbf{B}$ drift and the diamagnetic drift, let's consider equation 2.1, where a charged plasma is moving parallel to $\mathbf{E}$ and perpendicular to $\mathbf{B}$, while we still have the pressure gradient, $\boldsymbol{\nabla}p$. An scheme of the drift dynamics can be seen in figure 2.1, figure 2.1a for the $\mathbf{E} \times \mathbf{B}$ and figure 2.1b for the diamagnetic drift. We are interested in the movement of the guiding center. Therefore, we can

skip the reduction of the gyration of charge particles inside a magnetic field and solve equation 2.1 for a non varying velocity,

$$mn\frac{\mathrm{d}\mathbf{v}}{\mathrm{d}t} = qn(\mathbf{E} + \mathbf{v} \times \mathbf{B}) - \boldsymbol{\nabla}p = 0 \tag{2.2}$$
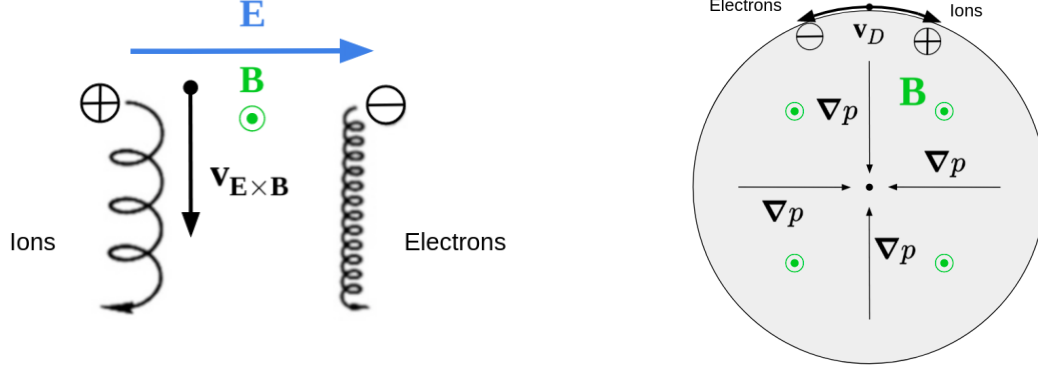
(a) Axis representation of the $\mathbf{E} \times \mathbf{B}$ drift.

(b) Axis representation of the diamagnetic drift.

Figure 2.1: Sketches of the $\mathbf{E} \times \mathbf{B}$ and diamagnetic drifts.

applying the cross product with $\mathbf{B}$, we get

$$qn\left(\mathbf{B} \times \mathbf{E} + \mathbf{B} \times (\mathbf{v} \times \mathbf{B})\right) - \mathbf{B} \times \boldsymbol{\nabla}p = qn\left(\mathbf{B} \times \mathbf{E} + \mathbf{v}B^2 - \mathbf{B}(\mathbf{v} \cdot \mathbf{B})\right) - \mathbf{B} \times \boldsymbol{\nabla}p = 0 \tag{2.3}$$

which can be rewritten as

$$\mathbf{v} = \frac{\mathbf{E} \times \mathbf{B}}{B^2} - \frac{\boldsymbol{\nabla}p \times \mathbf{B}}{qnB^2}. \tag{2.4}$$

Thus, we get two separated motions, the $\mathbf{E} \times \mathbf{B}$ drift, $\mathbf{v_{E \times B}}$,

$$\mathbf{v_{E \times B}} = \frac{\mathbf{E} \times \mathbf{B}}{B^2}, \tag{2.5}$$

and the diagmanetic drift, $\mathbf{v}_D$, which can be re-written by assuming an ideal gas with constant temperature, T, to erase the pressure,

$$\mathbf{v}_D = \frac{T}{qnB^2}\mathbf{B} \times \boldsymbol{\nabla}n. \tag{2.6}$$

It is important to highlight that temperature in nuclear fusion is written in electron volts, so that we insert Boltzmann's constant inside.

The $\mathbf{v_{E \times B}}$ shows that when a constant magnetic field and a constant electric field are applied over a moving particle, a part from the well known gyration motion, we also get a drift of the guiding center, in the direction perpendicular to the magnetic field and the electric field, completely independent of the charge.

The $\mathbf{v}_D$ is a consequence of the pressure gradient, this will push the fluid by moving the plasma in the direction perpendicular to $\mathbf{B}$ and $\boldsymbol{\nabla}p$. This generates a rotation current around the plasma, as the pressure gradient will always be pointing to the center of the reactor.

2.1.2   Polarization drift

The polarization drift is generated by a slowly time-varying electric field. To measure this, we will use perturbation theory over equation 2.1. Let's assume a velocity $\mathbf{v} = \mathbf{v}^{(0)} + \mathbf{v}^{(1)}$, where $\mathbf{v}^{(0)} = \mathbf{v_{E \times B}}$, such that the electric field varies slowly with time, but faster than $\mathbf{v}^{(1)}$. Hence, $\dfrac{\mathrm{d}\mathbf{v}^{(0)}}{\mathrm{d}t} \gg \dfrac{\mathrm{d}\mathbf{v}^{(1)}}{\mathrm{d}t}$. Thus,

$$m\frac{\mathrm{d}\mathbf{v_{E \times B}}}{\mathrm{d}t} = qn\left(\mathbf{E} + \mathbf{v_{E \times B}} \times \mathbf{B} + \mathbf{v}^{(1)} \times \mathbf{B}\right) - \boldsymbol{\nabla}p. \tag{2.7}$$

Notice that $\mathbf{E} + \mathbf{v}_{\mathbf{E} \times \mathbf{B}} \times \mathbf{B} = 0$, thus we can do the cross product with $\mathbf{B}$, as we did earlier,

$$m\frac{d\mathbf{E}}{dt} = qn\mathbf{v}^{(1)}\mathbf{B}^2 + \boldsymbol{\nabla}p \times \mathbf{B}. \tag{2.8}$$

Therefore, we see that $\mathbf{v}^{(1)} = \mathbf{v}_D + \mathbf{v}_p$, where

$$\mathbf{v}_p = \pm\frac{1}{\omega_c B}\frac{d\mathbf{E}}{dt}, \tag{2.9}$$

being ω_c the cyclotron frequency, $\omega_c = \frac{qB}{m}$. The $\pm$ sign refers to the charge of the particle, this drift will also contribute to the separation of charges.

As we can see, when we add a time-varying electric field, in addition to the already calculated $\mathbf{E} \times \mathbf{B}$ and diamagnetic drifts, we obtain perturbation that will move positively charged particles following the electric lines, while negative charged particles will move in the opposite direction, as we can see in figure 2.2. Hence, electrons and ions will move in opposite directions, separating from each other, while they follow the electric field.
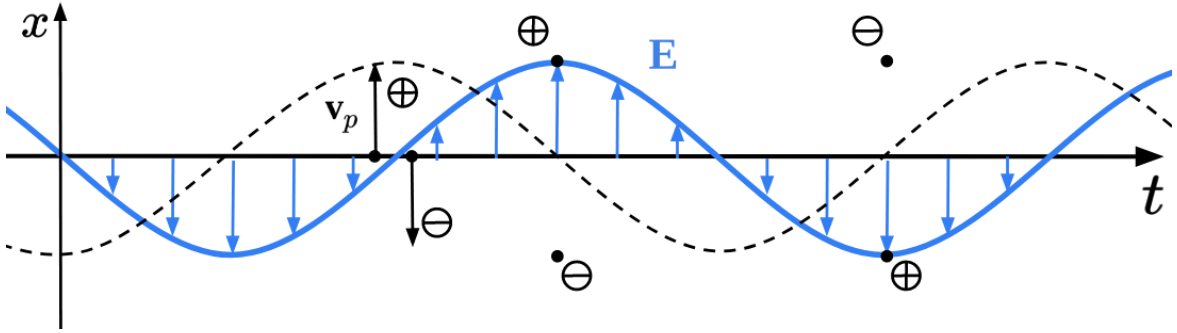

Figure 2.2: Sketch of the polarization drift.

2.2 Models, IC and HW and Phase relation

To study and characterize the turbulence at both sides of the last closed flux surface (LCFS), we will start by structuring a naive approach to the plasma dynamics. So that we can study separately the two main instabilities of interest, interchange (IC) [17] and Drift-Wave (DW) [18], [19]. Later, we shall put these two models together to construct a complete model and study both types of turbulence together [20].

The main reason to study these models is to verify the phase relation between potential and density. As it will be probed [21], [22], the IC turbulence transports plasma perfectly as the radial velocity gets in phase with the density, while in DW turbulence we have the contrary effect, radial velocity and density become out of phase. This property will allow us to characterize these 2 instabilities, but first we need to verify that our single models are able of probing this property.

For that propose, let's start by presenting the equations that will describe the dynamics of the system:

$$\frac{\partial n}{\partial t} + \boldsymbol{\nabla} \cdot (n\mathbf{v}) = 0, \tag{2.10}$$

$$\boldsymbol{\nabla} \cdot \mathbf{J} = 0, \tag{2.11}$$

$$\frac{1}{\eta}\left(\mathbf{E} + \frac{1}{nq}\boldsymbol{\nabla}p\right) = \mathbf{J}. \tag{2.12}$$

These equations are the mass continuity, charge density continuity equations and the Ohm's law respectively [5], [14], [16]. Where the only new parameters are the current density, $\mathbf{J}$, and the plasma resistivity, η. Notice that, we are only solving the equations for deuterium ions and electrons, the mass continuity equation is already simplified for a isothermal, quasi-neutral and cold ion plasma. Also, due to quasi-neutrality the charge density continuity equation is missing the time derivative of the density. The momentum conservation, equation 2.1, will be present, as we use it for deriving the drifts.

2.2.1   Interchange model

The first model we will derive is the Interchange model. This model will allow us to simulate the dynamics in the scrape-off layer (SOL) region and get interchange instability. First, we might assume some conditions, $T_i \ll T_e$, $T_e \approx$ constant, $m_i \gg m_e$ and $\omega_t \ll \omega_c$, where the e and i subindices refer to electrons and ions respectively and ω_t is the characteristic turbulence time variation. This allow us to fix the ion dynamics to the plane perpendicular to $\mathbf{B} = B_0 \hat{\mathbf{z}}$, as the ion inertia will fix particles in this direction and neglect thermal velocity of the ions. Hence, the transport of particles, for the mass continuity equation 2.10, can be assumed to be dominated by the $\mathbf{E} \times \mathbf{B}$ and diamagnetic drifts,

$$\mathbf{v} = \mathbf{v}_{\mathbf{E} \times \mathbf{B}} + \mathbf{v}_D = \frac{\mathbf{B} \times \boldsymbol{\nabla}\phi}{B^2} + \frac{T}{qnB^2}\mathbf{B} \times \boldsymbol{\nabla}n. \tag{2.13}$$

Further, we will erase the diamagnetic drift from the mass continuity equation as its contribution is neglectable for our case. Hence, the mass continuity equation becomes

$$\frac{\partial n}{\partial t} + \boldsymbol{\nabla} \cdot (n\mathbf{v}_{\mathbf{E} \times \mathbf{B}} + n\mathbf{v}_D) = \frac{\partial n}{\partial t} + \boldsymbol{\nabla} \cdot \left(n\frac{\mathbf{B} \times \boldsymbol{\nabla}\phi}{B^2} + \frac{T}{qB^2}\mathbf{B} \times \boldsymbol{\nabla}n \right) = 0. \tag{2.14}$$

This equation can be expanded as

$$\frac{\partial n}{\partial t} + \mathbf{v}_{\mathbf{E} \times \mathbf{B}} \cdot \boldsymbol{\nabla}n + n\boldsymbol{\nabla} \cdot \mathbf{v}_{\mathbf{E} \times \mathbf{B}} + \boldsymbol{\nabla} \cdot \frac{T}{qB^2}\mathbf{B} \times \boldsymbol{\nabla}n = 0. \tag{2.15}$$

This model is a fluctuation model, where instead of studying the whole density, we study the fluctuation n_1 over the background density n_0. Hence, we can write $n = n_0(1 + n_1)$, where $n_1 \ll 1$. Inside a reactor, the background density only varies with the radial direction [18], in our case the x direction, thus it gets canceled in the diamagnetic drift but not in the advection. Applying this and dividing by n_0, we get

$$\frac{1}{n_0}\left(\frac{\partial}{\partial t} + \mathbf{v}_{\mathbf{E} \times \mathbf{B}} \cdot \boldsymbol{\nabla} \right)\left[n_0(1 + n_1) \right] + \boldsymbol{\nabla} \cdot \mathbf{v}_{\mathbf{E} \times \mathbf{B}} + \boldsymbol{\nabla} \cdot \frac{T}{qB_0^2}\mathbf{B}_0 \times \boldsymbol{\nabla}\frac{n_0(1 + n_1)}{n_0} = 0, \tag{2.16}$$

which using the right transform and changing q by $-e$, the charge of the electron; we get

$$\left(\frac{\partial}{\partial t} + \mathbf{v}_{\mathbf{E} \times \mathbf{B}} \cdot \boldsymbol{\nabla} \right)(\ln n_0 + n_1) + \boldsymbol{\nabla} \cdot \mathbf{v}_{\mathbf{E} \times \mathbf{B}} - \boldsymbol{\nabla} \cdot \frac{T}{eB_0^2}\mathbf{B}_0 \times \boldsymbol{\nabla}n_1 = 0. \tag{2.17}$$

Before reducing this equation more, let's take a look at the charge density equation. The current density, $\mathbf{J}$, must be composed of all the drifts that separate charges, the diamagnetic and polarization drifts. Furthermore, we neglect parallel currents as the resistivity, η, in the parallel Ohm's law is supposed infinite, meaning that $\mathbf{J}$ must be perpendicular to $\mathbf{B}$. Thus, the charge density equation is expressed as

$$\boldsymbol{\nabla} \cdot \mathbf{J} = \boldsymbol{\nabla} \cdot \left(n\mathbf{v}_D + n\mathbf{v}_p \right) = 0, \tag{2.18}$$

where the polarization drift is defined like

$$\mathbf{v}_p = \frac{m}{qB^2}\left(\frac{\partial}{\partial t} + \mathbf{v}_{\mathbf{E} \times \mathbf{B}} \cdot \boldsymbol{\nabla} \right)\mathbf{E} = \frac{m}{eB^2}\left(\frac{\partial}{\partial t} + \mathbf{v}_{\mathbf{E} \times \mathbf{B}} \cdot \boldsymbol{\nabla} \right)\boldsymbol{\nabla}\phi. \tag{2.19}$$

Hence, the divergence of $n\mathbf{v}_p$ becomes,

$$\boldsymbol{\nabla} \cdot (n\mathbf{v}_p) = \boldsymbol{\nabla} \cdot \left[\frac{nm}{eB^2}\left(\frac{\partial}{\partial t} + \mathbf{v}_{\mathbf{E} \times \mathbf{B}} \cdot \boldsymbol{\nabla} \right)\boldsymbol{\nabla}\phi \right]. \tag{2.20}$$

In this case, we can assume that, as in the reactor $a/R_0 \ll 1$, the magnetic field is nearly constant $B \approx B_0$, and neglect the change in density so $n \approx n_0$. Furthermore, due to quasi-neutrality, we can neglect the divergence of $\mathbf{E}$, as Gauss's law gets

$$\boldsymbol{\nabla} \cdot \mathbf{E} = \rho/\varepsilon \approx 0, \tag{2.21}$$

where ρ is the charge density, $\rho \approx 0$ in a quasi-neutral gas, and ε is the electric permitivity. This allows us to move the divergence further in until $\boldsymbol{\nabla}\phi$.

Furthermore, we can define the vorticity density, ω, as

$$\frac{n_0}{B_0} \boldsymbol{\nabla} \cdot \boldsymbol{\nabla} \phi = \frac{n_0}{B_0} \nabla^2 \phi = \omega. \tag{2.22}$$

Notice, that the vorticity density can be demonstrated to be $\boldsymbol{\omega} = n_0 \boldsymbol{\nabla} \times \mathbf{v_{E \times B}}$, been a vector parallel to $\mathbf{B}$. This highlights the implication of this term and the physical relation of it.

Using the same steps we applied to get to equation 2.17, the current density equation, 2.11 is expressed as,

$$\boldsymbol{\nabla} \cdot \mathbf{J} = \boldsymbol{\nabla} \cdot (n\mathbf{v}_p + n\mathbf{v}_D) = \frac{m}{eB_0} \left(\frac{\partial}{\partial t} + \mathbf{v_{E \times B}} \cdot \boldsymbol{\nabla} \right) \omega - \boldsymbol{\nabla} \cdot \frac{T}{eB^2} \mathbf{B} \times \boldsymbol{\nabla} n_1 = 0, \tag{2.23}$$

which can be reduced to,

$$\left(\frac{\partial}{\partial t} + \mathbf{v_{E \times B}} \cdot \boldsymbol{\nabla} \right) \omega - \omega_c \frac{T}{e} \boldsymbol{\nabla} \cdot \frac{\mathbf{B}}{B^2} \times \boldsymbol{\nabla} n_1 = 0, \tag{2.24}$$

notice that, again, we have changed q by $-e$, the charge of the electron.

Finally, in equations 2.17 and 2.24 we have some terms we want to reduce, let's begin by solving the background density, $n_0(x)$, which generally is assumed to have a locally constant gradient. To do this, we shall assume n_0 to be an exponentially decaying profile [18], so that $n_0(x) \approx N_0 e^{-\frac{x}{L_n}}$, being L_n the characteristic length scale for the density gradient. Therefore,

$$\frac{\partial \ln N(x)}{\partial x} = -\frac{1}{L_n} \implies \left(\frac{\partial}{\partial t} + \mathbf{v_{v_{E \times B}}} \cdot \boldsymbol{\nabla} \right) \ln n_0(x) = \frac{1}{L_n B_0} \frac{\partial \phi}{\partial y} \tag{2.25}$$

Next, we need to take care of the cross products so that we can avoid having vectors in the equations. This means, dealing with the expressions of type

$$\boldsymbol{\nabla} \cdot \left(\frac{\mathbf{B} \times \boldsymbol{\nabla} \gamma}{B_0^2} \right), \tag{2.26}$$

where γ is used to denote both, the density and the potential, which is in both equations.

The magnetic field, which inside a torus is approximated as $B = B_0 \left(1 + \frac{a}{R_0} + \frac{x}{R_0} \right)$ [22], where x is the distance to the center. Furthermore, knowing that the magnetic field is proportional to the toroidal direction, we can write $\mathbf{B}/B = \hat{\mathbf{z}}$, the unitary vector perpendicular to our 2D system. Hence, we get

$$\boldsymbol{\nabla} \cdot \left(\frac{\mathbf{B} \times \boldsymbol{\nabla} \gamma}{B^2} \right) = \left(1 + \frac{a}{R_0} + \frac{x}{R_0} \right) \boldsymbol{\nabla} \cdot (\hat{\mathbf{z}} \times \boldsymbol{\nabla} \gamma) + (\hat{\mathbf{z}} \times \boldsymbol{\nabla} \gamma) \cdot \boldsymbol{\nabla} \left(1 + \frac{a}{R_0} + \frac{x}{R_0} \right) \tag{2.27}$$

which leads us to

$$\boldsymbol{\nabla} \cdot \left(\frac{\mathbf{B} \times \gamma}{B^2} \right) = -\frac{1}{B_0 R_0} \frac{\partial \gamma}{\partial y} = -\frac{\kappa}{B_0} \frac{\partial \gamma}{\partial y}, \tag{2.28}$$

where κ is the curvature of the magnetic field. This parameter is a key element for interchange turbulence, without it, we would get Euler's equation.

As it has already been mentioned, we wish to assume no diamagnetic drift compression [17]. Which is acceptable as $\mathbf{v_{E \times B}}$ is dominant over $\mathbf{v}_D$, been the drift that handles the plasma transport. Hence, the gradient of n_1 from equation 2.17 will be erased. Although it will appear when we escalate our model to a more complex one. For the vorticity equation, equation 2.24, this assumption is not valid, as we need charge separation for generating interchange instability. Therefore, our equations get simplified to,

$$\frac{n_0}{B_0} \nabla^2 \phi = \omega, \tag{2.29}$$

$$\left(\frac{\partial}{\partial t} + \mathbf{v_{E \times B}} \cdot \boldsymbol{\nabla} \right) \frac{n_1}{n_0} + \left(\frac{1}{L_n B_0} - \frac{\kappa}{B_0} \right) \frac{\partial}{\partial y} \phi = -\mu^2 \nabla^4 \frac{n_1}{n_0}, \tag{2.30}$$

$$\left(\frac{\partial}{\partial t} + \mathbf{v_{E \times B}} \cdot \boldsymbol{\nabla} \right) \omega + \frac{\omega_c T}{e B_0} \kappa \frac{\partial}{\partial y} n_1 = -\mu^2 \nabla^4 \omega. \tag{2.31}$$

Notice that we have add a diffusion term, actually hyperdiffusion term, for numerical stability, which is written as,

$$\nabla^4 = \boldsymbol{\nabla} \cdot \left[\boldsymbol{\nabla} \left(\boldsymbol{\nabla} \cdot \boldsymbol{\nabla} \gamma \right) \right] = \frac{\partial^4 \gamma}{\partial x^4} + \frac{\partial^4 \gamma}{\partial x^2 \partial y^2} + \frac{\partial^4 \gamma}{\partial y^4}. \tag{2.32}$$

This numerical term is added because turbulent flow generates eddies that tend to reduce into tinier scales, until they get dissipated, due to diffusion [23]. If we do not add a diffusion term, this swirls will continue decreasing into finer and tinier structures until infinity. This is only acceptable in an ideal physical scheme, but as we have a computational mesh, we cannot let this structures get lower than our grid size, meaning that we have to truncate them by adding numerical diffusion. In this case, hyperdiffusion is chosen as it improves stability [18], [24].

2.2.2   Drift-Wave model

The Drift-Wave turbulence model is based in the Hasegawa - Wakatani, proposed by Akari Hasegawa and Masahiro Wakatani for the first time in 1983 [25]. This model, allows us to study the Drift wave instability inside a magnetically confined plasma in the inner region, in a simple way, as simple as the Interchange model that we have already derived.

To make this model, we can do a really similar derivation as the one done for the interchange model, but this time we will not assume an infinite resistivity for the parallel Ohm's law. Hence, we introduce a current density $\mathbf{J}$ in the parallel direction for the electrons,

$$J_\parallel = -env_\parallel = \frac{1}{\eta} \left(\frac{1}{en} \boldsymbol{\nabla}_\parallel p + E_\parallel \right) = \frac{1}{\eta} \left(\frac{1}{en} \frac{\partial p}{\partial z} - \frac{\partial \phi}{\partial z} \right) \tag{2.33}$$

where we can apply the ideal gas equation again, $p = nT_e$, with T_e being constant; and apply the same approximations we have done earlier, $n = n_0(1 + n_1)$, where $n_1/n_0 \ll 1$. Hence,

$$J_\parallel \approx \frac{T_e}{e\eta} \frac{\partial}{\partial z} \left(n_1 - \frac{e\phi}{T_e} \right). \tag{2.34}$$

Now, the electron parallel current density will be introduced as the parallel velocity in both, the mass continuity equation 2.10 and the charge density continuity equation 2.11. For the continuity equation we do not need to add an ion parallel current, as we can assume that the ions are so heavy compared to the electrons that their inertia will maintain them in the plane perpendicular to $\hat{\mathbf{z}}$, similar to what we did for the IC model. Therefore, our equations will look similar as for the IC model,

$$\frac{\partial n}{\partial t} + \boldsymbol{\nabla} \cdot \left(n\mathbf{v}_{\mathbf{E} \times \mathbf{B}} + n\mathbf{v}_D - \frac{J_\parallel}{e}\hat{\mathbf{z}} \right) = 0 \tag{2.35}$$

$$\boldsymbol{\nabla} \cdot \left(n\mathbf{v}_D + n\mathbf{v}_p - \frac{J_\parallel}{e}\hat{\mathbf{z}} \right) = 0 \tag{2.36}$$

Now, there is only 2 things that will differ from what we did earlier. First, the magnetic curvature will be neglected, $\kappa = 0$. Inside the inner region of the reactor, the magnetic field can be assumed constant, $\mathbf{B} = B_0\hat{\mathbf{z}}$. Second, we have to deal with $\boldsymbol{\nabla} J_\parallel \hat{\mathbf{z}} = \frac{\partial J_\parallel}{\partial z}$. This will not create a big change, as for the curvature is just erasing the terms and for the gradient of $J_\parallel$ we get

$$\boldsymbol{\nabla} \cdot J_\parallel \hat{\mathbf{z}} = \frac{T_e}{\eta e} \frac{\partial^2}{\partial z^2} \left(n_1 - \frac{e\phi}{T_e} \right). \tag{2.37}$$

Introducing this term in equations 2.35 and 2.36 and doing the same derivation, we get

$$\left(\frac{\partial}{\partial t} + \mathbf{v}_{\mathbf{E} \times \mathbf{B}} \cdot \boldsymbol{\nabla} \right) \left(\frac{n_1}{n_0} \right) + \frac{1}{L_n B_0} \frac{\partial \phi}{\partial y} = -\frac{T_e}{\eta e^2 n_0} \frac{\partial^2}{\partial z^2} \left(\frac{e\phi}{T_e} - n_1 \right) - \frac{\mu^2}{B_0} \nabla^4 \omega. \tag{2.38}$$

$$\left(\frac{\partial}{\partial t} + \mathbf{v}_{\mathbf{E} \times \mathbf{B}} \cdot \boldsymbol{\nabla} \right) \left(\frac{\omega}{\omega_c} \right) = -\frac{T_e}{\eta e^2 n_0} \frac{\partial^2}{\partial z^2} \left(\frac{e\phi}{T_e} - n_1 \right) - \frac{\mu^2}{\omega_c B_0} \nabla^4 \omega. \tag{2.39}$$

The only term not yet clear is the second derivative with respect to z for the potential and the density. Based on the idea that particles should be constrained to move in the perpendicular

plane, no variable, except from the magnetic and electric fields, should have any dependency with it. Although, as we have discussed above, the Hasegawa - Wakatani model tries to simulate the dynamics of a plasma where particles can move freely along the magnetic field lines. For that reason, we can assume that n and ϕ will be locally described as plane wave in the z direction, this assumption is acceptable as long as n and ϕ are small enough,

$$n_1 = N_1 e^{i(kz - \omega_t t)} \tag{2.40}$$

$$\phi = \phi_0 e^{i(kz - \omega_t t)}, \tag{2.41}$$

where N_1 is the density amplitude, k and ω_t are the characteristic wave length and frequency. Doing this, we are forcing the modes to be unique, k. This will force zonal mode structures in the potential [26]. Thus, we can expressed our set of equations as,

$$\frac{n_0}{B_0} \nabla^2 \phi = \omega, \tag{2.42}$$

$$\left(\frac{\partial}{\partial t} + \mathbf{v_{E \times B}} \cdot \mathbf{\nabla} \right) \left(\frac{n_1}{n_0} \right) + \frac{1}{L_n B_0} \frac{\partial \phi}{\partial y} = \frac{T_e k^2}{\eta e^2 n_0} \left(\frac{e\phi}{T_e} - n_1 \right) - \frac{\mu^2}{B_0} \nabla^4 \frac{n_1}{n_0}, \tag{2.43}$$

$$\left(\frac{\partial}{\partial t} + \mathbf{v_{E \times B}} \cdot \mathbf{\nabla} \right) \left(\frac{\omega}{\omega_c} \right) = \frac{T_e k^2}{\eta e^2 n_0} \left(\frac{e\phi}{T_e} - n_1 \right) - \frac{\mu^2}{\omega_c B_0} \nabla^4 \omega. \tag{2.44}$$

The term $\left(\frac{e\phi}{T_e} - n_1 \right)$, which will be converted into $\left(\hat{\phi} - \hat{n} \right)$ after normalization, is written in the ordinary form. But we can rewrite this term to add zonal flow [19], [20], [26], by changing ϕ and n so that we only study the perturbation over them,

$$\hat{\phi} = \tilde{\phi} + \langle \hat{\phi} \rangle_y \tag{2.45}$$

$$\hat{n} = \tilde{n} + \langle \hat{n} \rangle_y \tag{2.46}$$

where $\tilde{\phi}$ and $\tilde{n}$ represent the perturbation over $\hat{\phi}$ and $\hat{n}$ and $\langle \cdot \rangle_y$ is the average over the poloidal direction y. Thus, the term $\left(\hat{\phi} - \hat{n} \right)$ becomes $\left(\tilde{\phi} - \tilde{n} \right) = \left[\hat{\phi} - \langle \hat{\phi} \rangle_y - \left(\hat{n} - \langle \hat{n} \rangle_y \right) \right]$.

2.2.3 Normalization

These equations are full of unknowns and parameters that we might not want to solve, as they could depend on each other or other parameters. Furthermore, solving the equations for a certain T_e or B_0 might not be ideal as this would depend on the reactor we are studying. To solve this issue, we must normalize our variables using Bohm normalization. There are different ways of doing this, depending on the variables we have, for that reason we shall follow the recipe depicted in [18],

$$\hat{x} = \frac{x}{\rho_s}, \ \hat{y} = \frac{y}{\rho_s}, \ \hat{t} = t\omega_c, \ \hat{\phi} = \frac{e\phi}{T_e}, \ \hat{n} = n_1, \ \hat{\omega} = \frac{\omega}{\omega_c} \text{ and } \hat{B} = \frac{B}{B_0}. \tag{2.47}$$

where ρ_s is the Larmor radius, defined as

$$\rho_s = \frac{\sqrt{T_e m_i}}{e B_0} = \sqrt{\frac{T_e}{e B_0 \omega_c}}. \tag{2.48}$$

Notice that the only free parameters of our equations are the temperature T_e and the magnetic field B_0.

Introducing this in the interchange model, equations 2.29, 2.30 and 2.31, we get,

$$\hat{\mathbf{\nabla}}^2 \hat{\phi} = \hat{\omega}, \tag{2.49}$$

$$\left(\frac{\partial}{\partial \hat{t}} + \hat{\mathbf{v}}_{\mathbf{E \times B}} \cdot \hat{\mathbf{\nabla}} \right) \hat{n} = \left(\frac{\rho_s}{R_0} - \frac{\rho_s}{L_n} \right) \frac{\partial}{\partial \hat{y}} \hat{\phi} - \frac{\mu^2}{\rho_s^4 \omega_c} \hat{\mathbf{\nabla}}^4 \hat{n}, \tag{2.50}$$

$$\left(\frac{\partial}{\partial \hat{t}} + \hat{\mathbf{v}}_{\mathbf{E \times B}} \cdot \hat{\mathbf{\nabla}} \right) \hat{\omega} = -\frac{\rho_s}{R_0} \frac{\partial}{\partial \hat{y}} \hat{n} - \frac{\mu^2}{\rho_s^4 \omega_c} \hat{\mathbf{\nabla}}^4 \hat{\omega}. \tag{2.51}$$

Now, we can re-define the different constants as,

$$g = \frac{\rho_s}{L_n}, \ \hat{\kappa} = \frac{\rho_s}{R_0} = \kappa\rho_s \text{ and } \nu = \frac{\mu^2}{\rho_s^4\omega_c}. \tag{2.52}$$

Also, we had our reasons for not modifying the advective term, we shall return to this later, but by now, let's simplify the equations by adding the Poisson brackets in the advective term,

$$\left(\hat{\mathbf{v}}_{\mathbf{E}\times\mathbf{B}} \cdot \hat{\boldsymbol{\nabla}}\right)\gamma = \frac{\partial\phi}{\partial x}\frac{\partial\gamma}{\partial y} - \frac{\partial\phi}{\partial y}\frac{\partial\gamma}{\partial x} = \{\phi, \gamma\}, \tag{2.53}$$

where, again, γ is just a random variable, either n nor ω.

Finally, we shall re-write the equation, getting rid of the hats,

$$\nabla^2\phi = \omega, \tag{2.54}$$

$$\frac{\partial n}{\partial t} = (\kappa - g)\frac{\partial\phi}{\partial y} + \{n, \phi\} - \nu\nabla^4 n, \tag{2.55}$$

$$\frac{\partial\omega}{\partial t} = -\kappa\frac{\partial n}{\partial y} + \{\omega, \phi\} - \nu\nabla^4\omega. \tag{2.56}$$

For the Hasegawa - Wakatani model, equations 2.42, 2.43 and 2.44, we get,

$$\hat{\nabla}^2\hat{\phi} = \hat{\omega}, \tag{2.57}$$

$$\left(\frac{\partial}{\partial\hat{t}} + \hat{\mathbf{v}}_{\mathbf{E}\times\mathbf{B}} \cdot \hat{\boldsymbol{\nabla}}\right)\hat{n} = -\frac{\rho_s}{L_n}\frac{\partial\hat{\phi}}{\partial\hat{y}} + \frac{T_e k^2}{\eta e^2 n_0 \omega_c}\left(\hat{\phi} - \hat{n}\right) - \frac{\mu^2}{\omega_c\rho_s^4}\hat{\nabla}^4\hat{n}, \tag{2.58}$$

$$\left(\frac{\partial}{\partial\hat{t}} + \hat{\mathbf{v}}_{\mathbf{E}\times\mathbf{B}} \cdot \hat{\boldsymbol{\nabla}}\right)\hat{\omega} = \frac{T_e k^2}{\eta e^2 n_0 \omega_c}\left(\hat{\phi} - \hat{n}\right) - \frac{\mu^2}{\omega_c\rho_s^4}\hat{\nabla}^4\hat{\omega}. \tag{2.59}$$

Again, rewriting our variables, we get

$$g = \frac{\rho_s}{L_n}, \ \alpha = \frac{T_e k^2}{\eta e^2 n_0 \omega_c} \text{ and } \nu = \frac{\mu^2}{\rho_s^4\omega_c}. \tag{2.60}$$

Hence, we can rewrite the ordinary Hasegawa - Wakatani in the same way we have already done with the interchange model:

$$\nabla^2\phi = \omega, \tag{2.61}$$

$$\frac{\partial n}{\partial t} = -g\frac{\partial\phi}{\partial y} + \alpha\left(\phi - n\right) + \{n, \phi\} - \nu\nabla^4 n, \tag{2.62}$$

$$\frac{\partial\omega}{\partial t} = \alpha\left(\phi - n\right) + \{\omega, \phi\} - \nu\nabla^4\omega, \tag{2.63}$$

and the modified Hasegawa - Wakatani model gets,

$$\nabla^2\phi = \omega, \tag{2.64}$$

$$\frac{\partial n}{\partial t} = -g\frac{\partial\phi}{\partial y} + \alpha\left(\tilde{\phi} - \tilde{n}\right) + \{n, \phi\} - \nu\nabla^4 n, \tag{2.65}$$

$$\frac{\partial\omega}{\partial t} = \alpha\left(\tilde{\phi} - \tilde{n}\right) + \{\omega, \phi\} - \nu\nabla^4\omega, \tag{2.66}$$

where $\tilde{n}$ and $\tilde{\phi}$ are defined as,

$$\tilde{\phi} = \phi - \langle\phi\rangle_y, \tag{2.67}$$

$$\tilde{n} = n - \langle n\rangle_y. \tag{2.68}$$

In our normalized models, we have now some new parameters that deserve a physical explanation. g is usually called the density profile and make particles move in the y direction. The term α is taken as an adiabatic constant by some authors [19], while others call it the plasma conductivity [20], which allows us to tune how strong the coupling between the potential and the density is.

2.2.4 Phase relation

Before continuing, as it has been already mentioned, we have to prove the phase relation between density and potential [21], [22]. As this will be our main approach to characterize and differentiate IC and DW instabilities. We can linearize the system by introducing the potential and density as simple plane waves of the form

$$n = N_0 e^{i(\mathbf{k} \cdot \mathbf{x} - \omega t)} \tag{2.69}$$

$$\phi = \phi_0 e^{i(\mathbf{k} \cdot \mathbf{x} - \omega t)} \tag{2.70}$$

inside the equations. Where N_0 and ϕ_0 are the amplitudes of the waves and $\mathbf{k}$ and ω are the characteristic wave number and frequency. Notice that $\omega = \omega_0 + i\gamma$, where the system will be unstable as far as $\gamma > 0$. This can only be done by assuming periodic boundaries in x and y. Hence, time derivative and spatial derivatives can be rewritten as $\frac{\partial}{\partial t} \to -i\omega$, $\frac{\partial}{\partial y} \to ik_y$ and $\boldsymbol{\nabla}^2 \to -k^2$.

Then, we can introduce this in the interchange model, equations 2.54, 2.55 and 2.56, where as this is an exact result we can erase the diffusion, getting,

$$-i\omega n = (\kappa - g) \, ik_y \phi, \tag{2.71}$$

$$i\omega k^2 \phi = -i\kappa k_y n. \tag{2.72}$$

where the relation between ϕ and n is,

$$N_0 e^{i(\mathbf{k} \cdot \mathbf{x} - \omega t)} = \pm k \sqrt{\frac{\kappa - g}{\kappa}} \phi_0 e^{i(\mathbf{k} \cdot \mathbf{x} - \omega t)}. \tag{2.73}$$

Here, we can extract the imaginary unit from the square root as $\kappa = \frac{\rho_s}{R_0}$, $g = \frac{\rho_s}{L_n}$. Where we know that $R_0 > L_n$, $\kappa < g$, as the length scale of the density gradient is lower than the mayor radius of the tokamak. Thus,

$$N_0 = \pm ik \sqrt{\frac{g - \kappa}{\kappa}} \phi_0. \tag{2.74}$$

Therefore, whenever the density is real, the potential must be purely imaginary and viceversa. Therefore, the phase relation becomes $\pm \frac{\pi}{2}$ rad. This causes an in phase relation between the radial velocity, $v_r = \mathbf{v_{E \times B}}x = \frac{\partial \phi}{\partial y}$, and the density, generating a 0 rad phase and perfect transport. This result is explained as interchange turbulence generates electric dipole moments.

It is important to notice that this result can only happen if the density equation dominates the evolution. This would only happen if $\omega_t \approx i\gamma$. This is, low frequencies, where the harmonic wave would be decaying or growing. In case this does not happen, the vorticity equation would become dominant. In this case, we see that ω and n become completely in phase, where ϕ and ω are in counter phase by $\pm \pi$. Thus, n and ϕ would also be in counter phase. In this case, we should see that the phase relation is not fulfilled along the whole grid.

If we do the same for the HW model, equations 2.61, 2.62 and 2.63, we get

$$-i\omega n = -ik_y g \phi + \alpha \left(\phi - n \right) \tag{2.75}$$

$$k^2 i\omega \phi = \alpha \left(\phi - n \right). \tag{2.76}$$

where, if the plasma conductivity is high enough to dominate, which is expected for a saturated state; the relation becomes

$$N_0 = -k^2 \phi_0 e^{i\theta}. \tag{2.77}$$

Hence, in a saturate drift-wave state, the potential and the density should be on phase by 0 rad. One could argue that minus can be considered as $e^{\pm i\pi}$ and say that n and ϕ should be out of phase by $\mp \pi$ rad. Although this is not the case. If we imagine a case where α tends to infinity, we should see that $\frac{\partial n}{\partial t} \approx \alpha \left(\phi - n \right)$, enforcing not only an in phase relation, but equalizing ϕ and n, for our unitless variables. Hence, we get inefficient plasma transport, as the phase between v_r and n becomes $\pm \frac{\pi}{2}$.

2.2.5   Complete model

If we want to study the behaviour of the plasma at both sides of the LCFS, we would need to put both, interchange and drift wave, models together. For that, we would like to use a more "complete" model, where we can study the inner part, were the drift wave turbulence is dominant, as well as the Scrape-Off Layer (SOL), where interchange turbulence is dominant. Thus, we will replicate use the model used by G. Decristoforo et. al. [20], with some changes,

$$\nabla^2 \phi = \omega, \tag{2.78}$$

$$\frac{dn}{dt} = -\kappa \left(\frac{\partial n}{\partial y} - n \frac{\partial \phi}{\partial y} \right) + \alpha(x)(\tilde{\phi} - n_1) + S_n(x, n) - \sigma(x) n e^{\Lambda - \phi} - \nu \nabla^4 n \tag{2.79}$$

$$\frac{d\omega}{dt} = -\frac{\kappa}{n} \frac{\partial n}{\partial y} + \alpha(x)(\tilde{\phi} - n_1) + \sigma(x) \left(1 - e^{\Lambda - \phi} \right) + S_\omega(x, n) - \nu \nabla^4 \omega \tag{2.80}$$

It is important to notice that this is not a fluctuation model anymore, which means that we look at the whole density, for that reason we have added a density source term S_n and variables are multiplied or divided by n to maintain the integrity of the whole system. It is interesting to highlight that we got rid of the density profile g, there is no background density, and we have recovered the diamagnetic drift, which was neglected earlier. For the vorticity we added a sink S_ω for stability proposes and to emulate the wall. Furthermore, we have added a sheath term $\sigma(x)e^{\Lambda - \phi}$, where σ is the sheath dissipation and Λ is the sheath potential.

The time derivatives are not partial derivative, this is because we define the total time derivative as,

$$\frac{d}{dt} = \frac{\partial}{\partial t} + \mathbf{v} \cdot \boldsymbol{\nabla} \tag{2.81}$$

where the speed $\mathbf{v}$ is defined as $\mathbf{v_{E \times B}}$, as it is the drift in charge of the transport. Later, the curvature velocity will be added when solving the density equation, which means that $\mathbf{v}_y = \mathbf{v_{E \times B}}_y + \kappa$. This will be done as part of the numerical solving method, which will add stability to the system. A further explanation will come in the next chapter.

As we have can see, some variables depend on x, the reason for this is the fact that the term that goes with the conductivity α only acts on the inner region inside the LCFS, as it has been explained, this term is made to approximate the particles that leave the 2D grid of the simulation by following the magnetic field lines towards z. After the LCFS the particles that follow the magnetic field lines will encounter the wall so this term does not have sense in the SOL. Furthermore, for this reason, we introduce a sheath term in the SOL, which is used to simulate the effect of the particles that get in the wall [27]. The source term is supposed to imitate the divertor and maintain the system with nuclear fuel, as particles will leave the system when entering the SOL. The curvature will be activated everywhere, meaning that we might find IC turbulence in the edge, in combination with DW turbulence, creating a mix region.

Hence, we can define mathematically the new and old variables, from left to write in the grid, as it is depicted in the schema of figure 2.3. First, we have the source term,

$$S_n(n, x) = \begin{cases} -\frac{n - n_b}{\tau}, & \text{if } x \leq x_a \\ 0, & \text{if } x > x_a \end{cases}, \tag{2.82}$$

where n_b is constant density that we want to be kept in the inner part, generally 1; τ is the relaxation time, how much does the source need to established any fluctuation; and x_a is the limit where the source is active, $x \in [0, x_a]$.

The vorticity sink as,

$$S_\omega(\omega, x) = \begin{cases} 0, & \text{if } x \leq x_c \\ -\frac{\omega}{\tau}, & \text{if } x > x_c \end{cases}, \tag{2.83}$$

where x_c is the left boundary of the sink, which is active until l_x, in case $x_c < l_x$.

The conductivity α is redefined as,

$$\alpha = \begin{cases} \alpha, & \text{if } x \leq x_b \\ 0, & \text{for } x > x_b \end{cases} \tag{2.84}$$
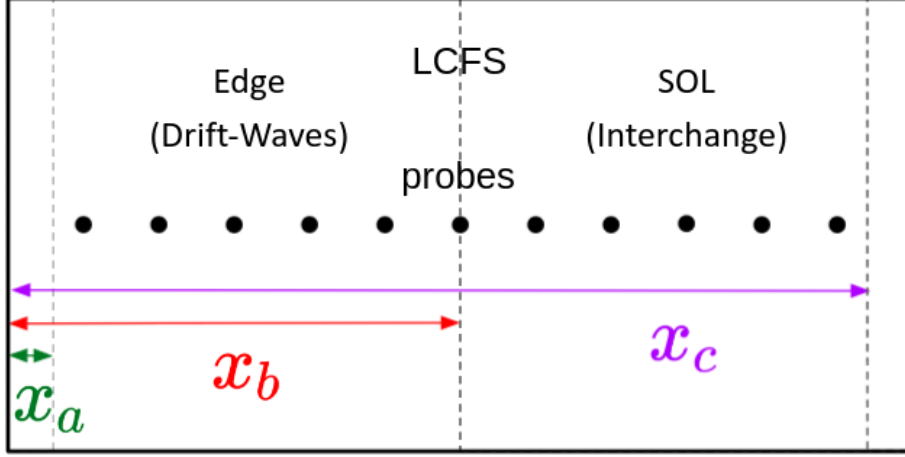
Figure 2.3: Grid representation of the Complete model.

where x_b is the location of the LCFS.

Finally, the sheath dissipation is written as,

$$\sigma = \begin{cases} 0, & \text{if } x \le x_b \\ \sigma, & \text{for } x_b < x < l_x \end{cases} \tag{2.85}$$

where l_x is the length of the grid in the x direction.

It is important to clarify that in the implementation it is not used a Heaviside step function to implement this behaviour, a hyperbolic tangent is used for this, $\tanh \frac{x - x_i}{w}$, where x_i is one of the three position, x_a, x_b and x_c, and w is the width of the hyperbolic tangent. This allows us to overlap both regions.

As it is seen in figure 2.3, a part from the spatial separation, we have also add some probes. The probes are used to measure some of the variables calculated in the simulation, we will get further in detail in the next chapter. In essence, these probes will allow us to characterize the turbulence inside the domain, they will be also used in the IC and HW models.

2.3   EAST reactor

The Institute of Plasma Physics in China has been using the EAST tokamak reactor, located in Heifei, to study the dynamics of the plasma by inserting probes [12]. The probe, as well as a scheme of the EAST reactor can be seen in figure 2.4a and 2.4b. Thanks to these experiments, it is possible to measure certain quantities of the plasma as density, plasma potential, radial velocity and temperature. The probes are inserted using a rail that allow them to enter and leave. For that reason, the measurements are done while the probe is moving. This also means that the probe measures when entering and when leaving, although we are not interesting in the signals when leaving the reactor, as they measure the perturbation created by the probe.

As seen in figure 2.4a, the probes have 3 tips to measure the floating potential, $\phi_f^{(1)}$, $\phi_f^{(2)}$ and $\phi_f^{(3)}$; a tip to measure the ion saturation current, I_{sat}, and a biased tip regarding I_{sat}, ϕ^+. These probes are placed so that non of them are aligned through the same magnetic field lines, this is the poloidal direction, as it is depicted in figure 2.5. For this reason, to get the floating potential in the same poloidal direction as ϕ^+ and I_{sat}, we have to average the floating potentials to get $\phi_f^{(12)}$ and $\phi_f^{(23)}$ signals,

$$\phi_f^{(ij)} = \frac{\phi_f^{(i)} + \phi_f^{(j)}}{2}, \tag{2.86}$$

where i and j refers to the pairs 1-2 and 2-3. Then, we can estimate the electron temperature by,

$$T_e \approx T_i \approx \frac{\phi^+ - \phi_f^{(12)}}{\ln(2)}, \tag{2.87}$$

(a) From [12], image of a probe used in the EAST experiments. The different tips are marked with the corresponding name of the obtained signal. The values $\phi_f^{(12)}$ and $\phi_f^{(23)}$ are not measured but obtained from averaging the signals from the corresponding upper and lower tips.
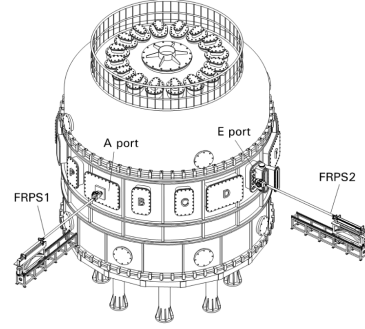
(b) From [21], scheme of the EAST reactor and the rails used to insert the probes inside of it.

Figure 2.4: Visualization of a probe used in the EAST experiments and the a scheme of the EAST reactor with the rails for the probes.
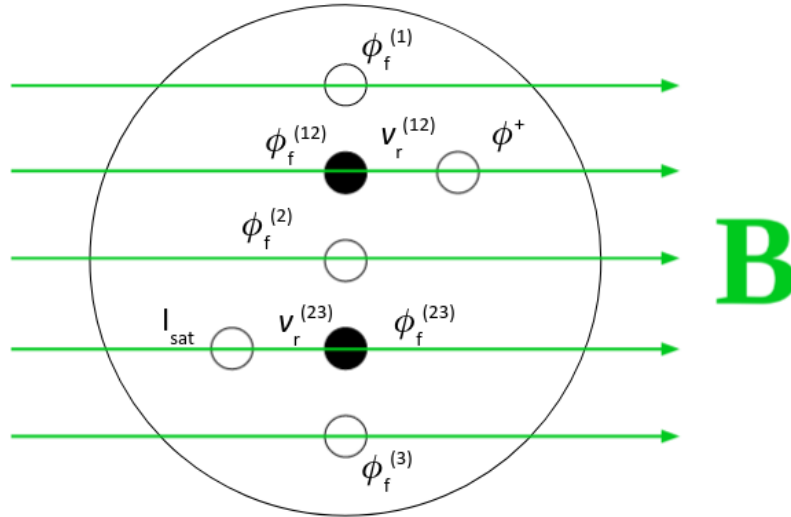

Figure 2.5: Scheme of the magnetic fields along a probe.

which can be used to calculate the plasma potential,

$$\phi_p = \phi_f^{(12)} + 3T_e, \tag{2.88}$$

where $3T_e$ is the sheath potential drop for deuterium plasma [12]. Then, we can calculate the plasma density, n, from the ion saturation tip, by

$$I_{sat} = enA_{eff}\sqrt{\frac{T_e}{2m_i}}, \tag{2.89}$$

with A_{eff} being the effective receiving area of the tip. To make this calculation acceptable one has to neglect electron temperature fluctuation effect, as T_e is not calculated in the same poloidal position as I_{sat}. Furthermore, the way these quantities are calculated make the plasma potential and the density dependant on the electron temperature. This is not ideal for our propose, but it is the best we can do, as we will be working with state-of-the-art data.
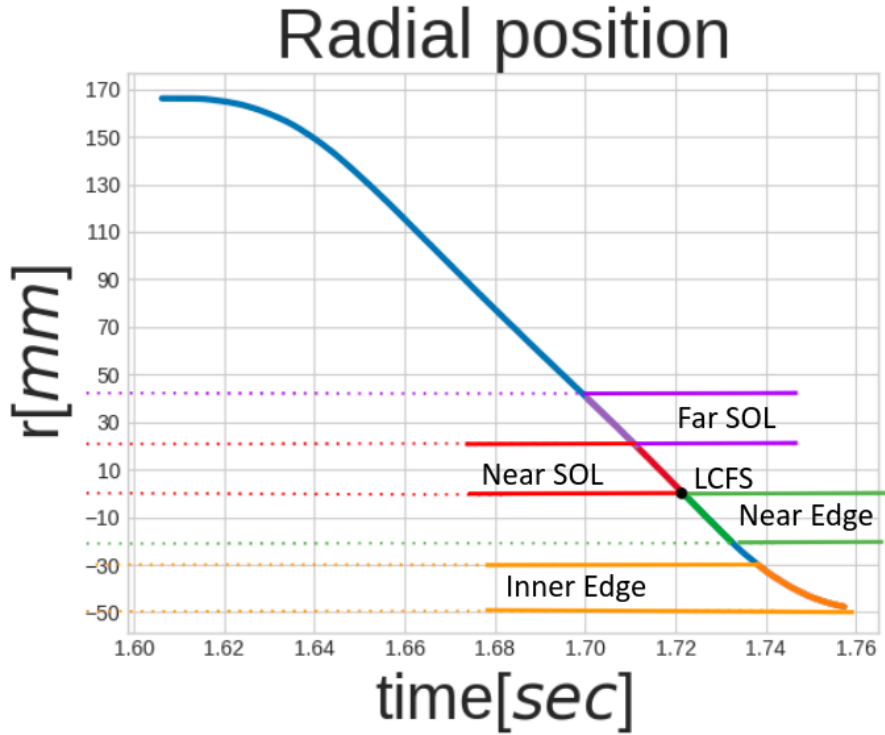
Figure 2.6: Radial position of the probe against time when inserted the probe. The the far SOL is between $r = 20$ and 40 mm; the near SOL is between $r = 0$ and 20 mm; the near edge is between $r = -20$ and 0 mm; and the inner edge is between $r = -20$ and -47.68 mm. The LCFS is at $r = 0$ mm.

Finally, we can also suggest to calculate the radial velocity, v_r, as

$$v_r^{(ij)} \approx \phi_f^{(i)} - \phi_f^{(j)}, \tag{2.90}$$

where similarly as in equation 2.86, the i and j parameters represent the floating potential pairs 2 and 1 and 2 and 3.

The rails allow to measure the plasma until the inner part of the reactor, a distance of more than 200 mm, until a distance of 47.68 mm pass the LCFS. For that reason, we need to choose which part of the data shall be studied. For that, knowing that the LCFS is located at 0 and the negative values are inside, we isolate the data in 4 different regions, as it is depicted in figure 2.6, the far SOL, $r \in [20, 40]$ mm; the near SOL, $r \in [0, 20]$ mm; the near edge, $r \in [-20, 0]$ mm; and the inner edge, $r \in [-20, -47.68]$ mm.

Chapter 3

Methods

The theory of the models used to approximate the physical system inside a tokamak have already been explained. Therefore, it is the moment to explain how are we going to solve the equations and study the result. We shall explain briefly how does the C++ library FELTOR (Full-F ELectromagnetic code in TORoidal geometry) [28] work and which analysis will be done to characterize the two main instabilities of interest.

3.1 Using FELTOR

The FELTOR library is a scientific software focused on using discontinuous Galerkin (dG) [29] methods to solve partial differential equations. FELTOR is platform independent and it allows the user to run the code in CPU and GPU without mayor changes than the compilation method. It also allows the introduction of the message passing interface (MPI) in a simple way. It is important to mention that as the FELTOR library is completely developed, the focus of these work has never been to get into detail on this methods. For that reason, dG methods were not mentioned during the theory. Although a brief explanation will be done here to satisfy the reader's curiosity, as well as a description of how FELTOR will be used to solve the models. This last part will be separated into 4 different sections, which time integration will be used, how will the program manage the advective acceleration, boundary conditions and input and output files.

The main work with FELTOR during this thesis was to create the models based on a previous work from [28], where the IC model was mostly implemented. The rest of the models were added to the implementation, as part of the work, with some changes to introduce MPI and the probe measurements. Nevertheless, the parallelization that MPI provides was not really used as the grid was never big enough to make a big different. For that reason, to accelerate the simulations, the code was migrated from the Marconi CPU cluster to the Marconi100 GPU cluster, without further adjustments due to the compatibility of FELTOR. The use of Marconi100 GPU cluster gave us an incredible computational power, although it limits to 24 h the maximum time a simulation can run. Also, we added the customized Python functions for analysing and animating the results that were completely developed from scratch, using the well known numpy, scipy and matplotlib libraries [30].

3.1.1 Discontinuous Galerkin methods

Galerkin methods are well known finite element methods to solve partial differential equations, dG methods are one of them [29], [31]. Discontinuous Galerkin methods are distinguished from the classical methods by the fact that they do not impose continuity between adjacent cells, while classical ones require continuity in the boundaries. Furthermore, dG methods can be used to solve elliptic equations and they are proved to improve the convergence, being able of achieving superconvergence [32].

Discontinuous Galerkin methods use Legendre polynomials in each cell to approximate the solution between the nodes. Legendre polynomials offer a wide variety of useful properties, specially for derivation,

$$\frac{x^2 - 1}{n} \frac{dP_n(x)}{dx} = xP_n(x) + P_{n-1}(x), \tag{3.1}$$

and integration, as we they are orthogonal in the [-1, 1] interval,

$$\int_{-1}^{1} P_n(x)P_m(x)dx = \frac{2}{2n+1}\delta_{nm}. \tag{3.2}$$

Hence, to approximate the solution, one has to define as many points as the degree of the used polynomial, between each node. These points can be placed randomly, but for convenience the Gaussian-Legendre quadrature points are chosen to ensure an easy integration,

$$\int_{-1}^{1} f(x)dx \approx \sum_{i=1}^{n} \omega_i f(x_i), \tag{3.3}$$

where f is any given function, ω_i is the quadrature weights, n is the number of points we have and x_i are the roots of a n-th degree Legendre polynomial. This solution is exact for any polynomial of order $2n - 1$.

Using these properties, the FELTOR library ensures an easy environment to solve the equations of our models. First, a grid must be defined, which can have Cartesian or cylindrical geometry, in our case Cartesian. The grid is done by defining the left and right boundaries, x0 and x1; lower and upper boundaries, y0 and y1, order of the Legendre polynomial, n; number of nodes per size, Nx and Ny, and the boundary conditions, bcx and bcy. This grid is then used to define the spatial derivative, and other operators, as matrices. This facilitates the assembly of the system, as, for example, we can sum all the terms, except from the time derivative, in equation 2.55 and then do the time integration to solve the density. Furthermore, if one is using different boundary conditions for the different variables, these can be specified when defining a matrix of a derivative operation.

3.1.2   Time integration

The time solver is really important as we need to maintain the code stable for as much as possible, allowing our system to reach a turbulent state. While doing this, one has to take into consideration the Courant–Friedrichs–Lewy (CFL) condition [33], or Courant condition, as breaking it would mean breaking the simulation. The CFL condition states that the speed of the information, $v_{info} = \Delta x/\Delta t$, has to be faster than the maximum speed in our system, v_{max}. Being Δx is the size between the nodes of our grid and Δt is the time step size. One can notice that v_{info} is the speed at which one updates the system. This relation is expressed as,

$$C = \frac{v_{max}\Delta t}{\Delta x} = \frac{v_{max}}{v_{info}} \leq C_{max} < 1, \tag{3.4}$$

where C is the Courant number and C_{max} is the maximum allowed ratio. Intuitively, one can see that if $v > v_{info}$, then the algorithm will not be able of updating the grid on time, losing information and making the simulation crash.

For the interchange and Hasegawa-Wakatani models, the karniadakis [34] time step was used, which has proven to be a really stable time solver for hydrodynamical systems. Karniadakis time integration is a 3rd order semi-implicit method used to integrate implicitly the viscosity term, to ensure stability. This scheme uses the 3 previous time steps for integration, making it light in terms of calculations, but heavy in terms of memory. For the complete model, 2 different solvers were used, an explicit 3rd order total variation bound "TVB-3-3" [35] multistepper and an adaptive time stepper "Bogacki-Shampine-4-2-3" [36]. The first method is a third order method, which uses the 3 latest time position to explicitly extrapolate the next one, for a constant time step. The second one is a third order Runge-Kutta embedded method, given a function an a time step, these methods gives back the error of the time integration along with the solution. Hence, one can estimate a time step as big as possible, so that the integration error is lower than a selected tolerance, avoiding breaking the CFL condition. For that, a part from an initial time step, we need to give the tolerance. Although the adaptive method allows us to optimize the time step, it does not do it for free. It needs to evaluate the system as many times as possible until it fulfils the convergence criterion, while the multistepper only evaluates the solution once. This change was made to ensure obtaining a turbulent state for the complete model, as it needed significantly more time units to evolve from the initial condition. In the complete model, the plasma velocity is slower, which allows to use a way bigger time step. Hence, it was decided to use the adaptive time stepper until a certain time unit and then let the instability grow with a fixed time step, so we could measure an evenly distributed time signal, which

is necessary to study the evolution. As one might notice, this change makes the system more sensible to the hyperdiffusion, as we are not solving it implicitly. However, total variation bound is more stable than karniadais [35].

3.1.3 Advective derivative

It is important to highlight how does the code deal with the advective derivative. As it has been stated, one can change the advection by a Poisson bracket. This can be seen in equation 2.53, which is written again,

$$\left(\hat{\mathbf{v}}_{\mathbf{E}\times\mathbf{B}} \cdot \hat{\boldsymbol{\nabla}}\right)\gamma = \frac{\partial\phi}{\partial x}\frac{\partial\gamma}{\partial y} - \frac{\partial\phi}{\partial y}\frac{\partial\gamma}{\partial x} = \{\phi, \gamma\}, \tag{3.5}$$

where γ is any given function, in our case either the density, n; nor the vorticity ω.

In the beginning, for the IC and HW models, we used the Arakawa's scheme for the Poisson brackets, which is directly calculating the derivatives and multiplying them. For the complete model this was changed, as during the process of this work, the FELTOR library was updated and the upwind discretization for the advection operation [24], [37] was introduced. This works by directly calculating the velocity first and multiplying it by the derivative, transforming equation 3.5 into,

$$\left(\hat{\mathbf{v}} \cdot \hat{\boldsymbol{\nabla}}\right)\gamma = v_x\frac{\partial\gamma}{\partial x} + v_y\frac{\partial\gamma}{\partial y}, \tag{3.6}$$

where we have substitute the $\mathbf{E}\times\mathbf{B}$ velocity by any velocity, $\hat{\mathbf{v}}$, as we commented in section 2.2.5. To the $\mathbf{E}\times\mathbf{B}$ velocity we will add the curvature in the density equations 2.55, 2.62, 2.65 and 2.79. This is done because the curvature goes with the term $\frac{\partial n}{\partial y}$. Hence, the velocity for each equation, the density and vorticity equations, becomes

$$\mathbf{v}_n = \mathbf{v}_{\mathbf{E}\times\mathbf{B}} + \mathbf{v}_\kappa = -\frac{\partial\phi}{\partial y}\hat{\boldsymbol{x}} + \left(\frac{\partial\phi}{\partial x} + \kappa\right)\hat{\boldsymbol{y}} \tag{3.7}$$

$$\mathbf{v}_\omega = \mathbf{v}_{\mathbf{E}\times\mathbf{B}} = -\frac{\partial\phi}{\partial y}\hat{\boldsymbol{x}} + \frac{\partial\phi}{\partial x}\hat{\boldsymbol{y}}, \tag{3.8}$$

where the subscripts n and ω represent each equation.

The upwind scheme looks at the sign of the velocity vector on each point of the grid. Then, it updates them using the nearest grid point from where the information comes from. This means, that if the x velocity is positive in a point, as the plasma goes from left to right, the point gets updated using only the value at the left.

At the end, this method was also use for the IC and HW models, as the radial velocity had to be saved. This decision was taken for stability propose and standardization. Although the first results were obtained using Arakawa's scheme, this was not the case when the simulations were re-run to include them in this report.

3.1.4 Boundary conditions

For the boundary conditions, in both cases, we will use periodic boundary conditions in the upper and lower boundaries, $y = 0$ and $y = l_y$. As we are looking at a tiny grid inside the reactor, we can just assume that the poloidal direction is symmetrical and, hence, statistically equal. For the right and left boundaries, $x = 0$ and $x = l_x$, we use Dirichlet boundary conditions for all three variables in the IC and HW models, $n(0, y) = n(l_x, y) = \omega(0, y) = \omega(l_x, y) = \phi(0, y) = \phi(l_x, y) = 0$. This allows us to confine the particles in the grid and not let them escape. Specially at the IC model, where due to the perfect transport mechanism, plasma would leave the grid fast. Furthermore, using Neumann boundary conditions at left and right boundaries makes the simulation unstable. For the complete model, we use Dirichlet boundary conditions at the left boundary for all three variables. For ω and ϕ we used $\omega(0, y) = \phi(0, y) = 0$, and for the density, due to the source, we use $n(0, y) = n_b$. In the right boundary, we used Dirichlet again for the potential, $\phi(l_x, y) = 0$ and Neumann boundary conditions for ω and n so that $\frac{\partial n}{\partial x}\Big|_{(l_x, y)} = \frac{\partial\omega}{\partial x}\Big|_{(l_x, y)} = 0$. As at the left boundary we have we have a source, we can expect to have fixed values of density, potential and vorticity. In the right boundary, we can lose density, then, the Neumann boundary conditions allows the density profile to evolve freely.

3.1.5   Input and output files

The input is written in a json file, while the output is written in Network Common Data Form version 4 (netCDF4). The json file makes it easy to introduce the initial conditions and define every variable. The initial condition is always introduced as a blob. The blob is defined as a Gaussian distribution for the density, and zero for ϕ and ω. A complete description and variable list can be found in the documentation [30], which is an extension from the one already written in the FELTOR library [28]. As a summary, the input file includes all the tunable variables of the code, spatial and time dimensions, initial conditions, parameters of the equations, accuracy for the spatial and time integration and the output grid. In the other size, the output file is separated in 2, as the program saves 2 out put files, one for the general values, grid, time, invariant variables and field variables, and another for the probes, where we save the positions of the probes and the values of the fields at those positions. The first netCDF4 file allows us to visualize the evolution of the system, while the second one allows us to make statistics.

One of the important properties of dG methods is that, a part from solving equation, it can also be used for interpolation. A quality that is used to reduce the data volume. In the simulation one uses the variables Nx, Ny and n to specify the grid size, nNx$\times$ nNy, during the simulation, and then the variables Nx_out, Ny_out and n_out, to specify the output grid size, n_outNx_out$\times$ n_outNy_out. Thus, before saving the field values, we interpolate into a less dense grid. Therefore, the fields are saved at lower resolution, while we do not make this interpolation for the probes.

3.2   Cross Power Spectral Density

One of the main jobs done during this thesis was the creation of the Python class analysis [30] and the many scripts to analyse and animate the output from the simulations. This can be seen in the Github repository (along with the FELTOR programs used in this project) [30]. In this Github directory one can find all the necessary code to run simulations and inspect, animate and analyse the results.

The key part of this code is the one focused on studying the phase difference between the density and the potential. We have already proved in section 2.2.4, that during drift wave turbulence, the potential and the density become on phase, 0 rad; and during interchange turbulence, they become out of phase by $\frac{\pi}{2}$ rad. The question is, how can we study this? One could make time cross-correlation, but this would only show the time that potential needs to catch up with density, and it is not that reliable. Hence, we propose to use the cross power spectral density (CPSD) as it has already been presented [22]. The CPSD is defined as the time cross correlation in the Fourier space [38]. Thus, if we have 2 real discrete signals $x(l)$ and $y(k)$, we can define the CPSD as the multiplication of both signals transformed,

$$CPSD(\omega) = \sum_{l=-\infty}^{\infty} x(l)e^{-i\omega l} \sum_{k=-\infty}^{\infty} y(k)e^{+i\omega k} = X(\omega)Y^*(\omega), \qquad (3.9)$$

where the higher case refers to the Fourier transform of the signals. This results in a complex function that, given a frequency, returns a complex value. The amplitude of this value refers to the contribution of that frequency and the complex value refers to the phase difference between the signals at that frequency. As it has been mentioned, we expect to get higher contribution for low frequencies with the already mentioned phase difference. The CPSD is implemented using the Scipy function csd from the signal package [39], [40].

To simplify this explanation, let's do a naive example. Considering 2 correlated signals, x and y. Which are defined as $x(t) = \sin{(\omega t)}$ and $y(t) = \sin{(\omega t + \varphi)}$, where ω is the angular frequency of both waves, $\omega = 2\pi$ rad/s; and φ is the phase difference, $\varphi = \frac{\pi}{4}$ rad. The angular frequency ω if related to a 1 Hz frequency. The signals are measured from 0 s to 5π s at a frequency of $f_s = 63.6$ Hz, which can be seen at the top of figure 3.1. From the CPSD of these 2 signals, we get the phase and amplitudes at the bottom left and right corners of figure 3.1 respectively. As we can see, the peak of amplitude, with a value of 1.48, is at $f = 1$ Hz. At that frequency, the phase difference is $\frac{\pi}{4}$ rad. This are the values of ω and φ we give to the signals. This means that the frequency with higher contribution is the frequency of both signals and the angle at that frequency is the phase relation between both signals. The rest of frequencies, the amplitudes decays, except from the nearest to $f = 1$ Hz, with values lower than 5 orders of magnitude lower. The rest of the frequencies do not contribute and are neglectable, as they are non-zero just because of boundary effects, the signals are not infinite.
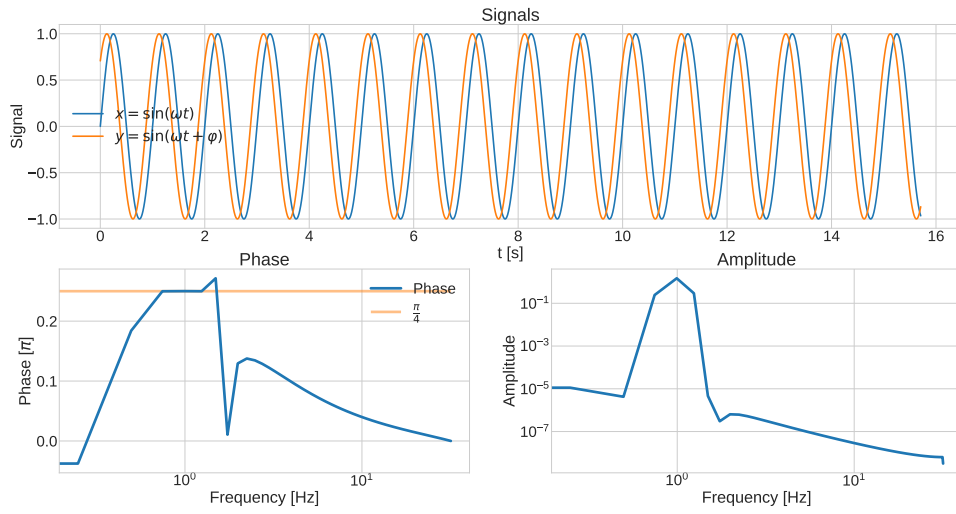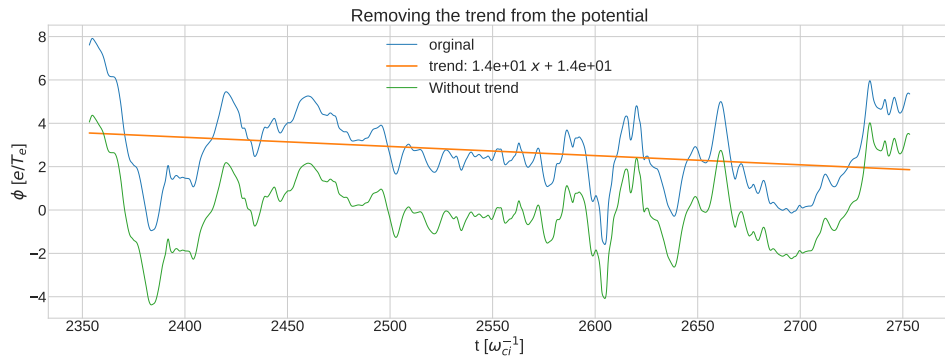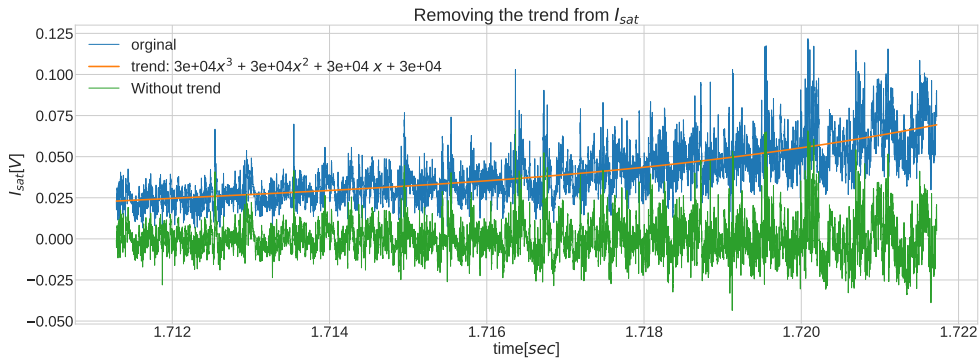
Figure 3.1: CPSD of 2 signals, in form of sines with angular frequency $\omega = 2\pi$ rad/s and phase difference $\varphi = \frac{\pi}{4}$ rad. At the top both signals are depicted, at bottom left the phase difference obtained from the CPSD is plotted and at the bottom right the amplitude from the CPSD is placed.

(a) Removing the linear trend of a potential probe from the IC model.

(b) Removing the high order trend of the I_{sat} signal.

Figure 3.2: Removing trend from both simulations and EAST probes

Similarly to this example, we will apply the CPSD to the output of the probes to calculate the phase relation. For that, we will take the time evolution of the density, potential and radial velocity, at the same spatial position and pre-process them. After the pre-processing, we will apply the CPSD to the potential with the density and to the radial velocity with the density. From this we should obtain the predicted phase relation between the variables, mainly for the low frequencies, which should have high contribution. We will do the same for the experimental data obtained from EAST and compare it.

For the pre-processing, first we need to isolate the signal at a quasi-stable state. Thus, we will erase the growing from the initial condition to a saturated turbulence state. Then, we have to erase any linear trend, or any higher order trend, from every probe. We want to focus on studying the turbulence in the system. The signals from the simulation have a linear trend that will be erased by making a linear regression and subtracting it from the signal, centering it around 0, as can be seen in figure 3.2a. For the experimental data from EAST, as there is a third order polynomial trend, we will use a polynomial fitting and subtract it from the signal, an example of this can be seen in figure 3.2b. Afterwards, we will average the phase relation in every probe along the x axis. To do so we need to do a weighted average with the contribution.

Chapter 4

Results

To verify this novel approach to study and characterize the turbulence at the near borders of the LCFS, three mayor experiments were conducted, one for each model, where it is expected to measure the phase difference between density and potential at a saturated turbulence state, as well as the phase relation for radial velocity and density. Furthermore, the same statistical measurements are going to be performed over the data obtained from EAST, at different regions, at both sides of the LCFS. First, we need to study the behaviour of turbulence at a saturate state. We need to verify that our simulations, over the interchange and Hasegawa-Wakatani models, the theoretical prediction is fulfilled and how. We will make both approaches equivalent by choosing similar parameters. Then, we need to apply the same study over the complete model to see how does the instability develop and how the result differs. Finally, we will do the same analysis with the data obtained from EAST.

Before starting, we must give account of the conversion of the time and spatial dimensions. For that, we will assume that we are only using deuterium and, for convinience, we will choose the Larmor radius, ρ_s, as 1 mm and the gyrofrequency as $\omega_c = 33.3$ rad MHz, meaning that 1 time unit $= 1 \, \omega_c^{-1} = 30$ ns. Hence, the magnetic field results in $B = 0.696$ T, which is bit low, and the electron temperatures becomes $T_e = 23.215$ eV, which is the same as 269,402.24 K.

4.1 Verification experiments

For the verification experiments, we will choose similar variables for both models, the only 2 variables that are not in common are the magnetic curvature, κ, and the plasma conductivity, α. For the spatial and time dimension, we choose $dt = 0.0025 \, \omega_c^{-1} \approx 75$ ps, $l_x = 64 \, \rho_s \approx 64$ mm, $l_y = 128 \, \rho_s \approx 128$ mm, with the same $l_x : l_y$ relation for Nx:Ny, Nx=128, Ny=256. The time step is the time separation between measurements for the probes, this means that the measurement frequency will be $f = 13.3$ GHz. To measure the potential, density, vorticity and radial velocity time evolution, we placed 100 probes along the radial axis, x, at the center of the poloidal direction, $y = 64$ mm. The separation between them will not be even, as the grid is not evenly distributed and we displayed 100 probes along $3 \times 64 = 196$ grid points. The density profile, g, and the viscosity, μ, are chosen $g = 1.0$ and $\mu = 10^{-4}$. In table 4.1, we can see all the shared variables by both models, with a little description. If one wants to reproduce these experiments, the input files, with these settings, can be found in the folder /Feltor_2D_Master_Thesis/FELTOR-model/ in the Github repository [30]. The names of the input files are input_IC.json, input_HW_mod.json and input_HW_ord.json, where one only needs to choose κ or α, by changing the variables curvature or adiabatic, respectively.

4.1.1 Interchange model

Although, both experiments were done at the same time, we will start with the interchange model, equations 2.55, 2.54 and 2.56, as it was the first one to be implemented. The only free parameter we have left with is the curvature, κ. For that, we made three experiments with $\kappa = \{0.06, 0.015, 0.00375\}$. A last moment error was made when performing these simulations, the time step was selected to $dt = 0.001 \, \omega_c^{-1} = 30$ ps, and the grid dimensions were doubled in each axis. This does not change the result in a significant way, the only change is in the measurement frequency, as it increases to $f = 33.3$ GHz.

Name	Type	Value	Description
n	integer	3	Gaussian nodes in x and y
Nx	integer	128	grid points in x
Ny	integer	256	grid points in y
dt	integer	0.0025	time step in units of ω_c^{-1}
n_out	integer	3	Gaussian nodes in x and y in output
Nx_out	integer	32	grid points in x in output fields
Ny_out	integer	64	grid points in y in output fields
itstp	integer	200	steps between outputs
eps_pol	float	1e-5	accuracy of polarisation solver
eps_time	float	1e-6	accuracy of implicit time-stepper
stages	integer	3	of stages in the multigrid algorithm (Nx and Ny have to be divisable by 2**stages)
dens_prof	float	1	Density profile g
nu_perp	float	1e-4	pependicular viscosity ν
amplitude	float	0.5	amplitude A of the blob
sigma	float	1	blob radius σ
posX	float	0.5	blob x-position in units of l_x, i.e. $X = p_x l_x$
posY	float	0.5	blob y-position in units of l_y, i.e. $Y = p_y l_y$
lx	float	64	l_x
ly	float	128	l_y
bc_x	char	"DIR"	boundary condition in x (one of PER, DIR, NEU, DIR_NEU or NEU_DIR)
bc_y	char	"PER"	boundary condition in y (one of PER, DIR, NEU, DIR_NEU or NEU_DIR)

Table 4.1: Common variables used for the interchange and Hasegawa-Wakatani model.

The main point of doing these three experiments was to show the relation of κ with the phase relation, as higher the curvature higher the coupling between density and radial velocity. Instead of that, we got an unexpected results. For the three values of κ we got similar results as the one seen in figure 4.1, where from left to right we have the potential, density and vorticity shown for $\kappa = 0.015$ at time $t = 1800\omega_c^{-1} = 54\,\mu s$. Due to the Dirichlet boundary conditions, when the initial blob is ejected to the right boundary, the plasma is reflected back generating two big convective cells, which can be clearly seen in the potential, left graph from 4.1. It is important to mention that we can not see tiny structures in the potential as it is a global variable, in contrast with density or vorticity which are local variables. The big convective cells generate a dipole moment in the interface between them, as they have opposite electric potential. This equipartition turbulent state is well known and has already been studied [41]. The two big convective cells dominate the transport of the system and only allow the plasma to be transported form left to right and vice versa by thin streams between the cells. This equipartition turbulence is caused mainly due to a high Reynolds number, which is caused by the too high viscosity, which could not be reduced due to stability. The streams between the vortexes can be easily seem in the density snapshot, central image of figure 4.1. From the streams it is interesting to notice that the lower one has negative density, and it is moving to the left, while the one in the higher part has positive density, and it is moving to the right. The negative one is probably a hole, which would explain why the density is negative and it moves backwards. As seen in the vorticity, right image in figure 4.1, between both there is also really turbulent zones, which are the one we need for our study. Still, this is a problem, we might not be able of measuring the turbulent zones with the probes. The interface between vortexes might not be centered in the middle where we had our probes, seen as the dots in the middle of every graph in figure 4.1. Not all the probes are plotted, as we used 100, they would look just as a straight line, hence only 20 are depicted. Also, we shall not forget that the density shows a growing gradient, from left to right, which is mainly generated from the density gradient g.

To avoid the creation of this equipartition turbulence, studies with different $l_x : l_y$ were also done, which resulted in the union of both vortexes creating a periodic mode with transport mainly in the poloidal direction [42]. In this regime, there is nor radial transport, reason why it was decided to not include these results.
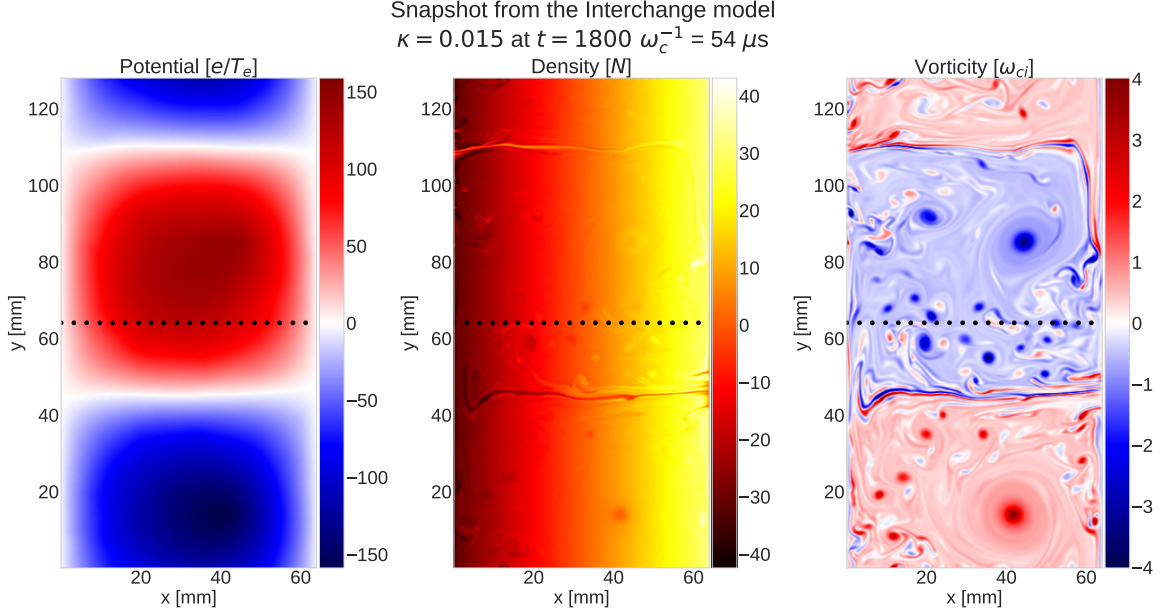
Figure 4.1: Snapshot of the Rayleigh-Taylor instability in magnetically confined plasma obtained using the interchange model, with $\kappa = 0.015$ at time 1800 ω_c^{-1}=54 µs. From left to right, the potential, density and vorticity are shown. At the center of each we can see 20 of the probes used.

To study the phase difference between the potential and the density, as well as between the radial velocity and the potential, the simulations were run as long as possible, so that the system can reach a quasi-stable state. From all of the signals we erase the last 5 % for the study, mainly because some of the simulations crash as they broke the CFL condition. This mainly happened in the complete model, but as an standardization method we did it for every simulation. From the remaining, we use the last 12 µs for the statistics. This means that for the CPSD we use 160,000 points, 400,000 when using $dt = 0.001$, of every probe signal ensuring the statistical robustness.

From each probe we see a signal similar to the ones seen at the top of figure 4.2, where we can see the normalize density and normalize potential against time, in the top left corner; and the normalize density and normalize radial velocity against time, in the top right corner. The normalization is done by erasing the linear trend and dividing by the highest number of the signal, for the density we used a lower value, to make it easier to visualize. In both cases the signal is taken in the central position of the grid, $x = 32.56$ mm, for the last 0.9 µs of the simulation done with $\kappa = 0.015$. In the signals, it is difficult to see the phase relation, density has a really high frequency, while the potential and the radial velocity have much slower time evolution. However, when we look at the solution from the CPSD, we can see that the lowest frequencies have the largest contribution, top right of figure 4.2. Where from 0 MHz until 100 MHz, we have that the peaks of contribution decreases 1 order of magnitude, afterwards, the amplitudes become neglectable. At those frequencies, we obtain a phase relation between ϕ and n, bottom left corner, that disagrees with the theoretical result, around $\frac{\pi}{4}$ rad. This discrepancy is seen more ore less everywhere, and might be caused by the vortexes. For the phase shift between v_r and n, bottom right corner, we have the expected 0 rad relation. Thus, when averaging the phase at every radial position, we expect to see nearly straight line for the radial position at 0 rad and a varying curve for the potential.

In figure 4.3 it is depicted the average phase relation between the potential and the density, top; and between the radial velocity and the density, bottom. The phase relation between potential and density for $\kappa = 0.00375$ and 0.015 the phase seems to be generally 0 rad, disagreeing the theoretical result, for the center of the grid, at the boundaries there are some changes. For $\kappa = 0.06$, we can see that in the center the grid, between $x = 15$ to 45 mm, the phase oscillates around $\frac{\pi}{2}$ rad. This suggests that, for $kappa = 0.00375$ and 0.015, the probes might be measuring the vortexes more than the turbulence, while for $\kappa = 0.06$, it might be measuring the turbulence, at least part of it. Another reason might be that the coupling is not that strong as κ is not high enough. However, it is important to notice that the big convective cells rotate synchronized for all the variables, which means that potential and density are in phase, in these regions. While the boundary effects are probably
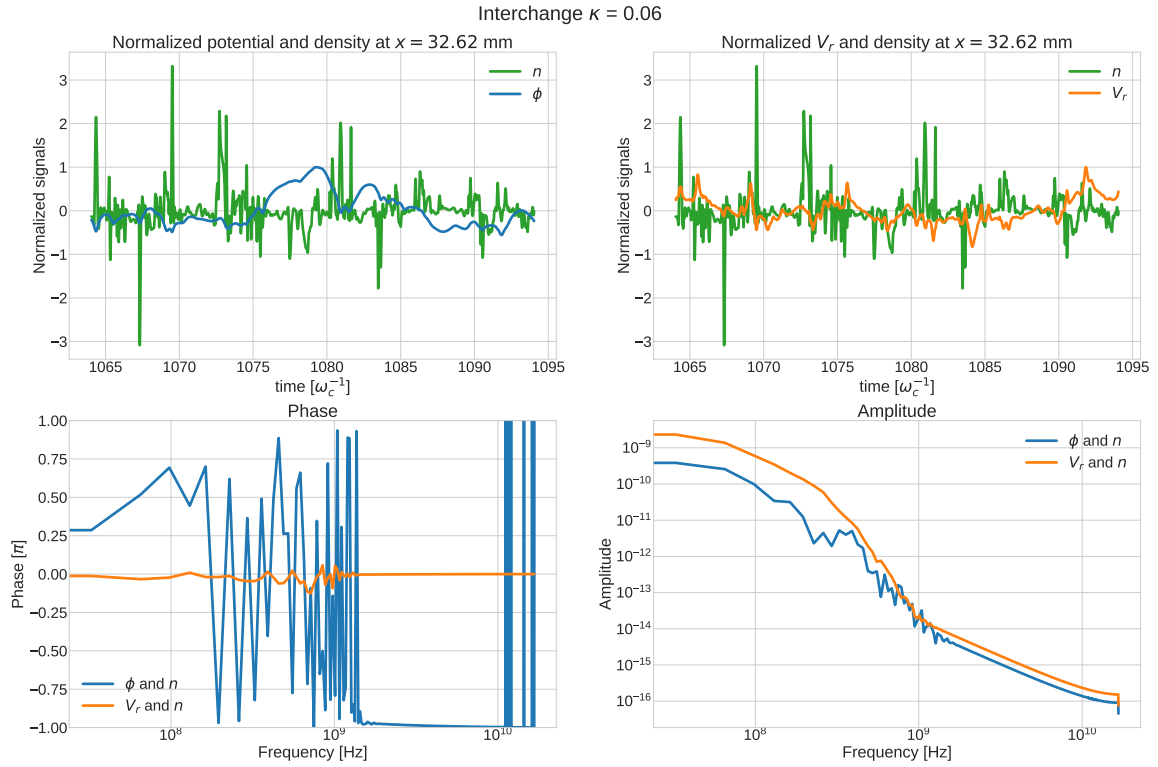
Figure 4.2: From the interchange model: normalized potential and density, top left; normalized radial velocity and density, top right; phase relation between potential and density, bottom left; and between radial velocity and density, bottom right.
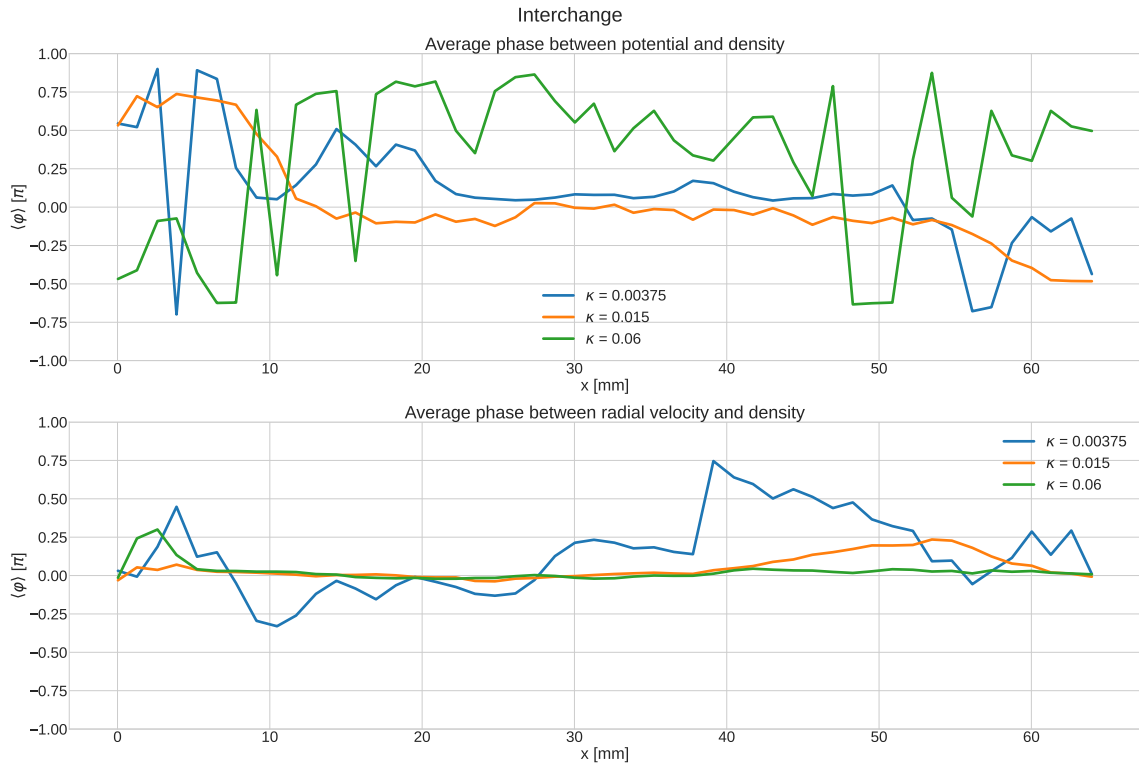

Figure 4.3: Phase relation between potential and density, top; and between radial velocity and density for the interchange model.

related to the fact that the streams that transport plasma radially, get thicker at the extremes. The most interesting result is seen for the radial velocity, as there we can see that for all the values of κ, we measure a 0 rad phase relation everywhere, except for $\kappa = 0.00375$ between $x = 37$ to 50 mm. The reason for this change in the phase for $\kappa = 0.00375$ is unclear, after analysing the time evolution of that simulation, we could suggest that it may be related to a perturbation of the system by a hole. As it has been already mention, holes are places with low density that move backwards to the expected. Still, we do not see any significant change when we look at the average phase between ϕ and n. Hence, further investigation should be done, as this could be an interesting result. However, the fact that, when analyzing the phase between the radial velocity and the density, we still get 0 rad, means that even with equipartition turbulence, the transport is perfect for IC. Not measuring the theoretical result for the potential is mostly related to the fact that this phase is related to the creation of dipole moments. The two big vortexes create a big dipole moment. This big dipole moment might only be measured at the interface of the convective cells, where turbulence dominate and the stream are placed. Hence, when measuring inside a cell, plasma might not be perturbed by the dipole moment, getting synchronized with the vortexes. Inside the vortexes the electric potential becomes really high and due to periodic boundary conditions, this dipole moment might be cancelled. Also, it is important to remind that the linearization we made to predict the phase shift was done assuming periodic boundary conditions, while we use Dirichlet boundary conditions for these simulations. Thus, these results match the expected.

4.1.2 Hasegawa - Wakatani model

In case of the Hasegawa-Wakatani model, we realized that the ordinary model fails in stability and could not be used successfully for this project. Hence, from now on, only the modified HW model will be used, equations 2.64, 2.65 and 2.63, even for the complete model. In this case, the only free parameter is the plasma conductivity, α. We also performed 3 simulations, with $\alpha = [0.2, 0.05, 0.0125]$.
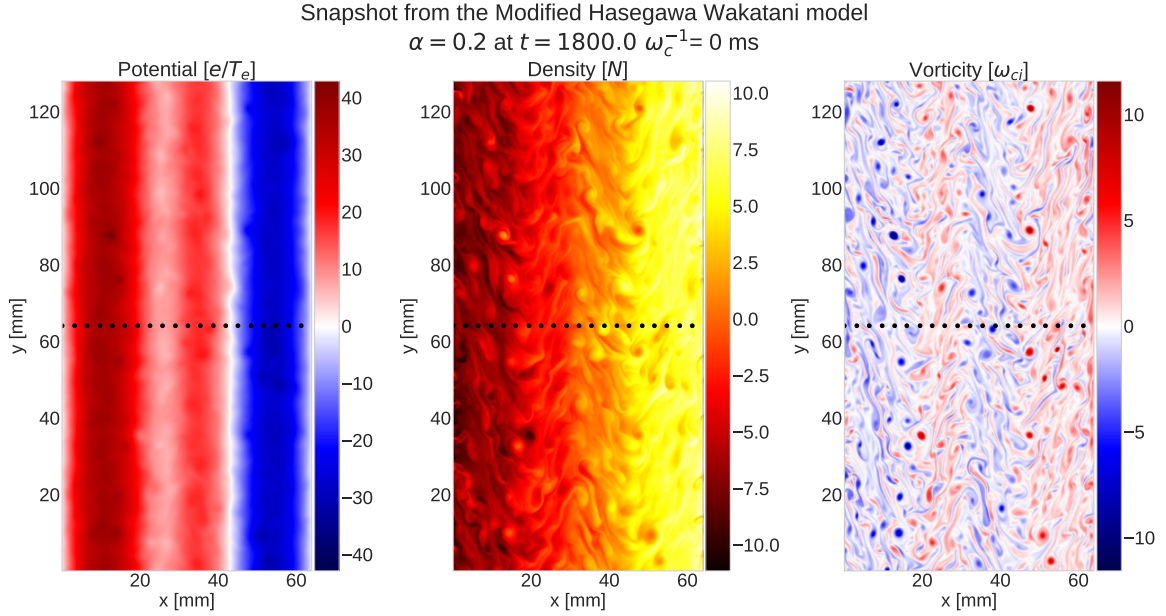

Figure 4.4: Snapshot of the Drift-Wave instability in magnetically confined plasma obtained using the modified Hasegawa Wakatani model, with $\alpha = 0.2$ at time $1800 \, \omega_c^{-1} = 54 \, \mu s$. At the center of each we can see 20 of the probes used.

From these simulations, we obtained the expected drift-wave turbulence, which is seen in figure 4.4, from left to right: the potential, density and vorticity. In this snapshot of the evolution of the system, we can see the DW turbulence for a plasma conductivity $\alpha = 0.05$ at time $t = 1800 \, \omega_c^{-1} = 54 \, \mu s$. For the other values of α we get a similar result. As for the IC model, the dots in the center are the probes, were we have only plotted a fifth of them, the rest are in the same poloidal position. In this case the evolution is quite different, as DW is not a perfect transport mechanism, we do not see the blob ejected to the right boundary. At the beginning of the simulation, the blob starts developing eddies

that are propagated all around the grid until it generates the structures we can seen in figure 4.4. As in the IC model, the potential does not represent the tiny eddies seen in the density or the tiny vortexes seen in the vorticity. Still we can see zonal models on it, which are seen as columns, also visible for the vorticity [26]. Also, we have again a growing gradient in the density, caused by g. As the turbulence is propagated everywhere, we can be sure that we will measure it with the probes. Hence, the results from the probes should agree with the theoretical results regardless the position of the probe.
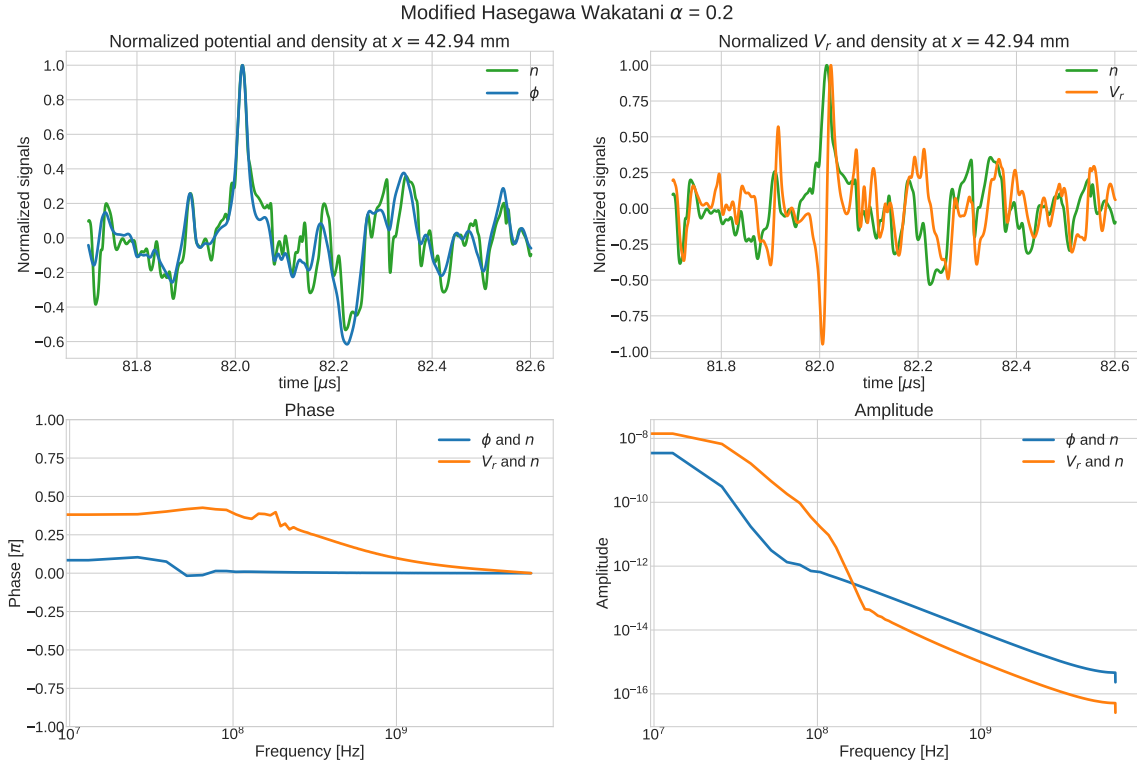

Figure 4.5: From the modified Hasegawa-Wakatani model: normalized potential and density, top left; normalized radial velocity and density, top right; phase relation between potential and density, bottom left; and between radial velocity and density, bottom right.

To analyse the solution we do the same as we did for the IC model, erase the last 5 % of the signal and use the last 12 µs. Similarly, as we did before, in figure 4.5, we can see an example of the signals obtained from the probes and the solution from the CPSD. The signals, seen at the top of the figure, are more clear than the ones seen in figure 4.2. If we inspect the graph in the top left corner, we can see that the density and the potential are completely in phase, with some shifts for high frequency peaks. The tendency of the signals, the low frequency oscillations, are completely in phase. This is translated to 0 rad phase difference between density and potential, as seen at the bottom left corner, for all the frequency spectrum. This is followed with high contribution of the low frequencies, as seen in the graph in the bottom right corner, where the maximum is around 10^{-10} and then it decays really fast, nearly two orders of magnitude lower at 10 MHz. For the radial velocity, at the lower right corner, we can see that the overall peaks are always a bit shifted, they are not in phase. This is translated with nearly a $\frac{\pi}{3}$ rad phase. In this case, the amplitude has the same tendency, the peak is at nearly 10^{-9} and then it decreases, not as fast as for the potential. Again, we expect a similar tendency for all the probe. For that, we will plot the average phase for each radial position, so we can see the overall phase.

In figure 4.6 we can see the average phase between potential and density, top; and radial velocity and density, bottom. The average phase between potential and density looks exactly as the prediction, except for some boundary effects. The phase is basically 0 rad everywhere but the boundaries. This means that, as we have seen in figure 4.5, the potential and the density are completely in phase, independently of the conductivity. The phase relation between radial velocity and density, seems more interesting. When we look at it, we can see that when we increase α the uncoupling is larger,

for $\alpha = 0.2$, we get a signal with an absolute value that oscillates getting values between $\frac{\pi}{3}$ and $\frac{\pi}{2}$ rad. The change of sign is not significant, still, it is important to highlight, that it is created due to the zonal modes. The zonal mode columns in the vorticity have opposite signs, which create this change in sign. When we look at lower values of α, we see that for $\alpha = 0.05$, this tendency is still remaining, specially in the right side, but the oscillations are more frequent and the values are not that well defined. The same happens with $\alpha = 0.0125$, it is hard to decide if the average phase is worse or better, in terms of the prediction. Zonal modes are not that well defined for these two cases, which emphasizes these oscillations. However, the phase difference between potential and density fulfills the prediction for all the simulations and we should expect that increasing α should fix the phase difference between v_r and n to the prediction. Which shows that the transport during DW instability is inefficient.
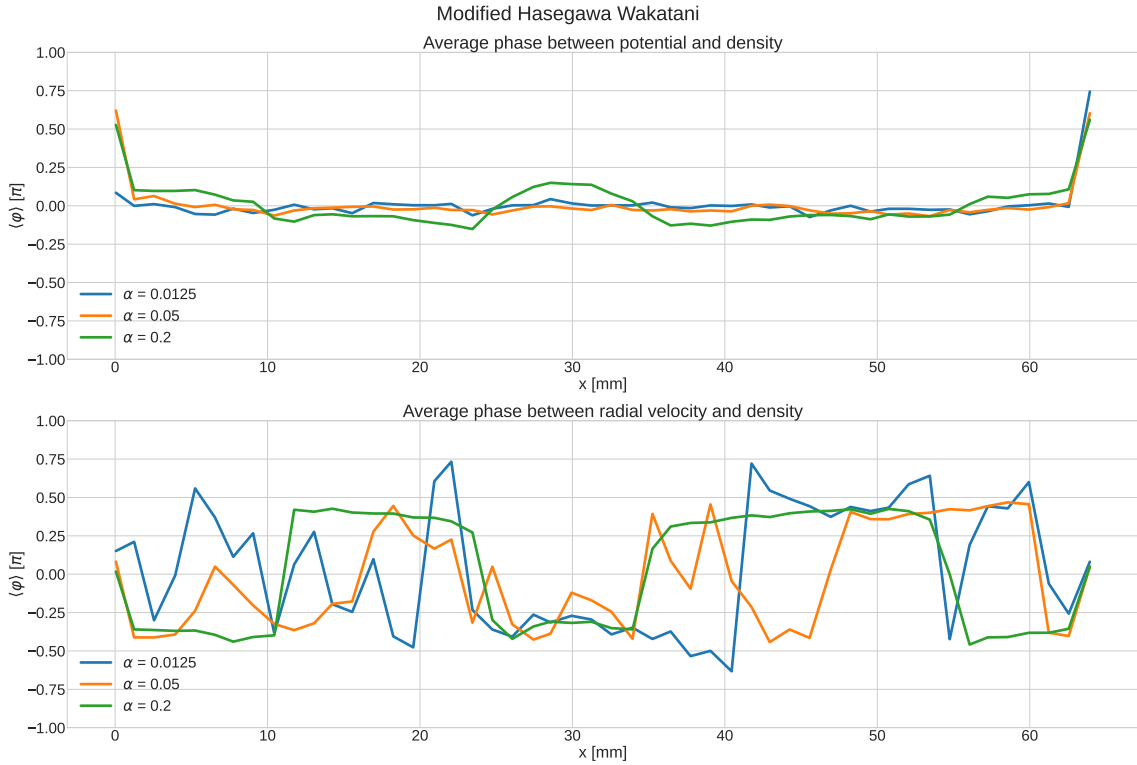

Figure 4.6: Phase relation between potential and density, top; and between radial velocity and density for the modified Hasegawa Wakatani model.

4.2 Characterisation of turbulence in the Complete model

After probing our theoretical results using the separate models, IC and HW, it is the moment to test the complete model, equations 2.78, 2.79 and 2.80. For that, as we did earlier, we will fix every variable except from α, allowing us to show how this variable controls the phase relation between potential and density in the edge. Higher α, higher the coupling and the nearer the phase to 0 rad. The fixed variables are $dt = 0.1\ \omega_c^{-1} \approx 3$ ns, $l_x = 200\ \rho_s = 200$ mm, $l_y = 100\ \rho_s = 100$ mm, with the same $l_x : l_y$ relation for N_x:N_y, N_x=200, N_y=100. The time step is the time separation between measurements for the probes, thus, the measurement frequency will be $f = 333.3$ MHz. The curvature, κ; the viscosity, ν; the sheath dissipation, σ; and the sheath potential, Λ; are chosen $\kappa = 0.0015$, $\nu = 2 \cdot 10^{-5}$, $\sigma = 5 \cdot 10^{-5}$ and $\Lambda = 0$. The source term is activated in the region between $x = 0$ mm and $x_a = 10$ mm, with a characteristic time scale of $\tau = 50\ \omega_c^{-1} = 1.5\,\mu$s. The LCFS is at $x_b = 100$ mm, separating the edge and the scrape-off layer. The vorticity is damped at $x_c = 190$ mm. The rest of the variables, can be seem in the table 4.2, there is also an input field, called `input_Complete.json`, in the github repository, in the folder /Feltor_2D_Master_Thesis/FELTOR-Complete/ [30], in case one wants to reproduce the result. The non-fixed variable, the conductivity, will be defined as $\alpha = \{0.01, 0.005, 0.001, 0.0005\}$. It is important to notice that $\alpha = 0.05$, the center

of the interval in the HW experiments, is not taken as it makes the simulation unstable, it is too big and it breaks the CFL condition fast, which would force us to reduce the time step, with no satisfactory result.

Name	Type	Value	Description
Time_step	char	"Mixed"	Specifying the time integration (multistepper, adaptive or mixed)
Time_change	float	75000	Time for the change from adaptive to multistepper in mixed Time_step
n	integer	3	Gaussian nodes in x and y
Nx	integer	128	grid points in x
Ny	integer	256	grid points in y
dt	integer	0.0025	time step in units of ω_c^{-1}
n_out	integer	3	Gaussian nodes in x and y in output
Nx_out	integer	32	grid points in x in output fields
Ny_out	integer	64	grid points in y in output fields
itstp	integer	200	steps between outputs
eps_pol	float	1e-5	accuracy of polarisation solver
eps_time	float	1e-6	accuracy of implicit time-stepper
stages	integer	3	of stages in the multigrid algorithm (Nx and Ny have to be divisable by 2**stages)
curvature	float	0.015	Magnetic curvature κ
sheath_diss	float	5e-5	Sheath disspation term $\sigma(x)$
sheath_pot	float	0	Sheath potential Λ
tau	float	50	Relaxation term τ for the source S_n
nb	float	50	Constant term n_b for the source S_n
nu_perp	float	1e-4	pependicular viscosity ν
amplitude	float	0.5	amplitude A of the blob
sigma	float	1	blob radius σ
posX	float	0.5	blob x-position in units of l_x, i.e. $X = p_x l_x$
posY	float	0.5	blob y-position in units of l_y, i.e. $Y = p_y l_y$
lx	float	64	l_x
ly	float	128	l_y
tanh_width	float	0.001	thickness of the boundary between IC and HW
x_a	float	1/3	x_a: delimiter for the source term. It has to be a float betwen 0 and 1, so that the actual value os x_a * lx
x_b	float	2/3	x_b: delimiter between IC and HW. It has to be a float betwen 0 and 1, so that the actual value os x_b * lx
bc_x_n	char	"DIR"	boundary condition in x for the density (one of PER, DIR, NEU, DIR_NEU or NEU_DIR)
bc_x_omega	char	"DIR"	boundary condition in x for the vorticity (one of PER, DIR, NEU, DIR_NEU or NEU_DIR)
bc_x_phi	char	"DIR"	boundary condition in x for the potential (one of PER, DIR, NEU, DIR_NEU or NEU_DIR)
bc_y_n	char	"PER"	boundary condition in y for the density (one of PER, DIR, NEU, DIR_NEU or NEU_DIR)
bc_y_omega	char	"PER"	boundary condition in y for the vorticity (one of PER, DIR, NEU, DIR_NEU or NEU_DIR)
bc_y_phi	char	"PER"	boundary condition in y for the potential (one of PER, DIR, NEU, DIR_NEU or NEU_DIR)

Table 4.2: Variables used for the complete model.

There are three things to appreciate here. First, at the beginning of the experiment, the adaptive time stepper is used until $t = 75000 \ \omega_c^{-1} = 2.25$ ms. In this interval the time step, dt, is not fixed, afterwards it will become 3 ns. As it has been explained, this is done to increase the speed of evolution and reach a turbulent quasi-stable state. Second, the number of points per space unit has decrease
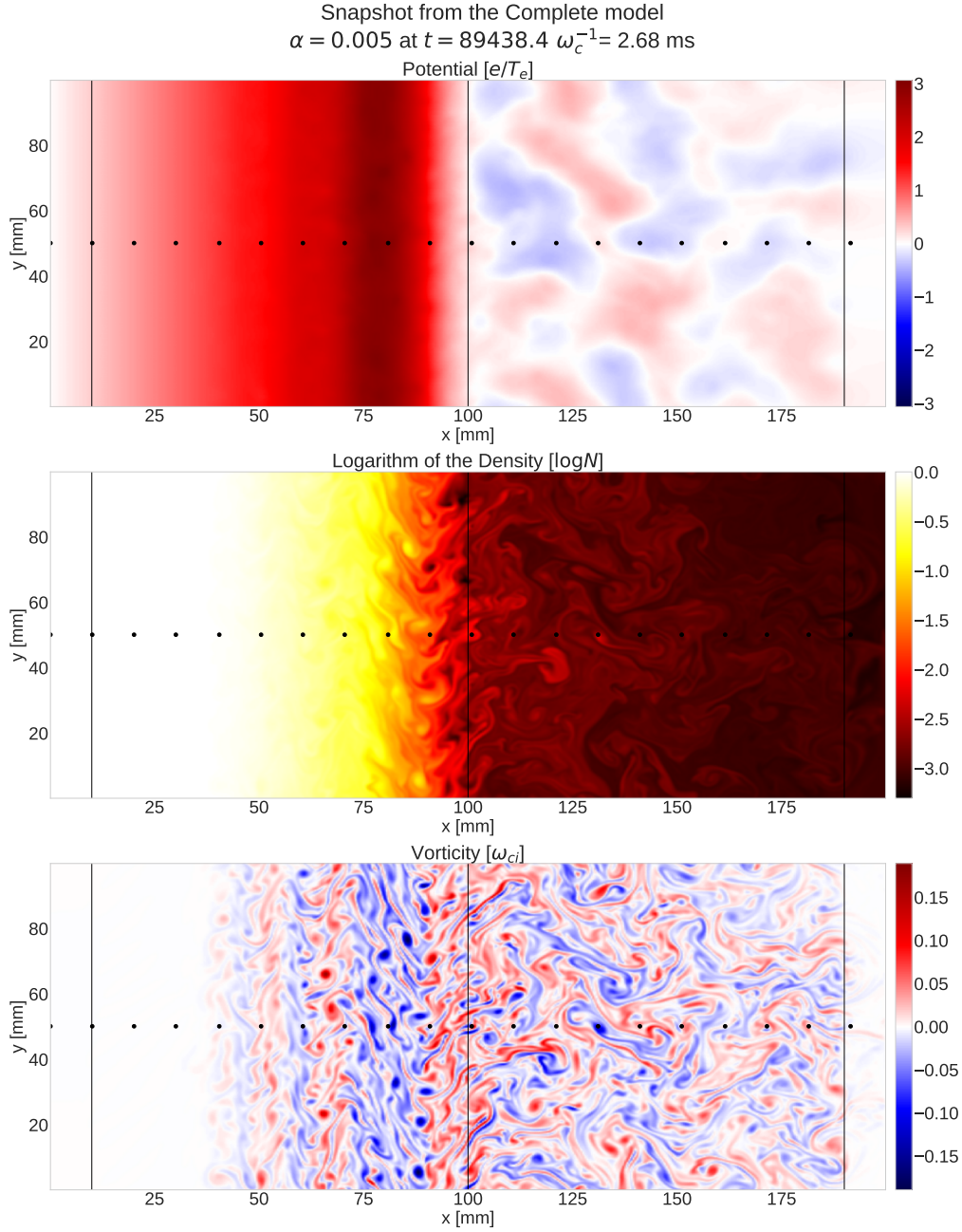
Figure 4.7: Snapshot of the plasma dynamics in magnetically confined plasma obtained using the complete model, with $\alpha = 0.005$ at time $89438.4 \ \omega_c^{-1} = 2.68$ ms. At the center of each we can see 20 of the probes used.

to half the value, using the same relation as for the original models we could have had a grid of 1200×600, this is computationally too expensive and unaffordable, the time a simulation can run in Marconi100 is limited. Third, the viscosity, ν, is 5 times lower. Due to the stability of this simulation, we were able of reducing the numerical diffusion.

As it happens with the IC and HW models, the view of the output does not change that much. Thus, we can discuss the evolution of the system with just a snapshot in the quasi-stable state of one simulation. In figure 4.7 we can see, from top to bottom, a picture of the potential, the logarithm of the density and the vorticity, after 2.68 ms, from the simulation with $\alpha = 0.005$. Instead of the n, we plotted $\log n$, as now n is positive define, and it makes the structures easier to see. The vertical lines represent, from left to right, x_a, x_b and x_c. The dots in the center are the probes, as we did earlier, we only plotted 20 of the 100 used, all of them are in the same poloidal position. The vertical

lines will also appear in every plot where the x axis is present. There are some interesting things to notice from these plots. If we look at the potential, top, we can see that in the edge there are no structures, although in some of the simulations we can see the zonal modes in the potential in the form of vertical straight structures [26]. In this picture the zonal modes are not that clear, but the high potential vertical column near the LCFS is a consequence of this. In the density, center, it is interesting to notice that, although half the edge seems to be full of vortexes, as seen in the vorticity, bottom; due to the n source, the turbulence is hided from $x = 0$ mm to $x \approx 75$ mm. Afterwards, between $x = 75$ mm and the LCFS, $x = 100$ mm, we can see really high instability, generated by the interface of both models, where a big gradient of density is noticeable. Thus, we can see how the region with close magnetic lines is able of confining the plasma with high density, while a low dense part is emitted along the SOL. The plasma that is emitted, in our case, is just sent to the wall, were we can see really clearly the IC turbulence, with the mushroom characteristic shape structures. The vorticity, even if we do not use it for our analysis, becomes a clear way of visualizing how far is the turbulence propagated, in this case, it is not propagated all over the grid, which is a topic highly discussed in the bibliography [43], and could be a topic of interest for the future. Also, we can see some columns before the LCFS, where we can see that maxima and minima of vorticity are separated, these columns trouble up and down, as a consequence of zonal flow.
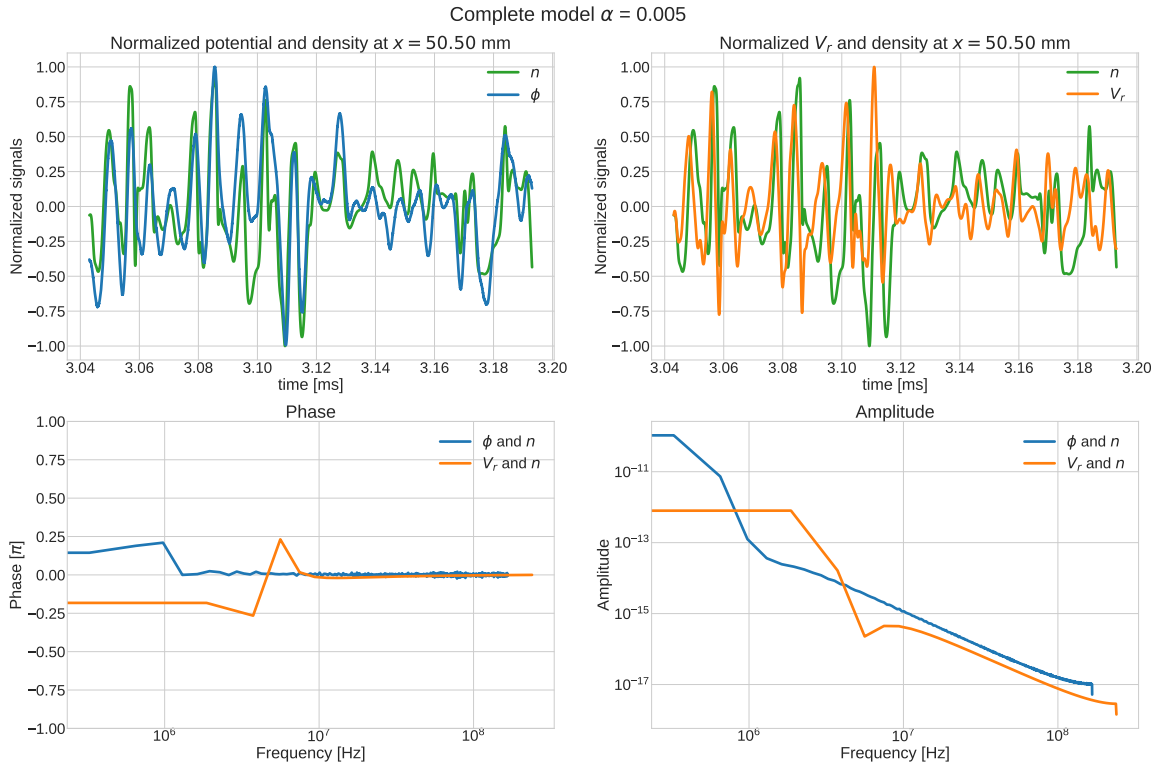

Figure 4.8: From the complete model in the edge: normalized potential and density, top left; normalized radial velocity and density, top right; phase relation between potential and density, bottom left; and between radial velocity and density, bottom right.

To study the phase differences, we will first plot the signals obtained by the probes. As we have already done before, we will only look at one probe, in the interval we use for the average phase relation. In this case, as it has been mentioned, most the simulations with this model ended before the expected as they broke the CFL condition, although we damped the vorticity to ensure stability. For this reason, the treatment of the data will be done by erasing the last 5 % and taking the last $150\,\mu s$, 50000 measurements from each probe, of the remaining. In this case, we have 100 probes placed along the center, as seen in figure 4.7, as evenly distributed as possible. Before looking the average, we shall look at the signals, which will be done by first looking the signals in the edge, at $x = 50.50$ mm, figure 4.8; and then in the SOL region, at $x = 141.11$ mm, figure 4.9. This will be done for the simulation with $\alpha = 0.005$. In both cases, we can see the whole analysed signal, as the fluctuations are slower than for the IC and HW models.

In figure 4.8 we can see the normalized potential and density, top left corner. Here, we can see that the fluctuations for both variables are completely in phase for nearly the whole evolution. Although some of the peaks are a bit shifted. For this reason, when we look at the phase difference, bottom left corner, we can see that it is not exactly 0 rad, but it does not grow more than 0.15π rad, where the contribution as already decay almost 2 orders of magnitude. The amplitude, bottom right corner, as expected, has the maximum value for the lowest frequency, around 10^{-12} and it decays quite fast. For the phase between radial velocity and density, we can see that the peaks are always shifted, the density seems to be following the radial velocity, top left corner. This is reflected as an almost $-\frac{\pi}{4}$ rad phase between both, for the lowest frequencies, which are the ones with higher contribution. The contribution is a bit different from the one between density and potential, the maxima are at the lowest frequencies and it stays straight till 1.3 MHz and then it decays quite fast. Thus, along the edge we might see the average phase relation variate.
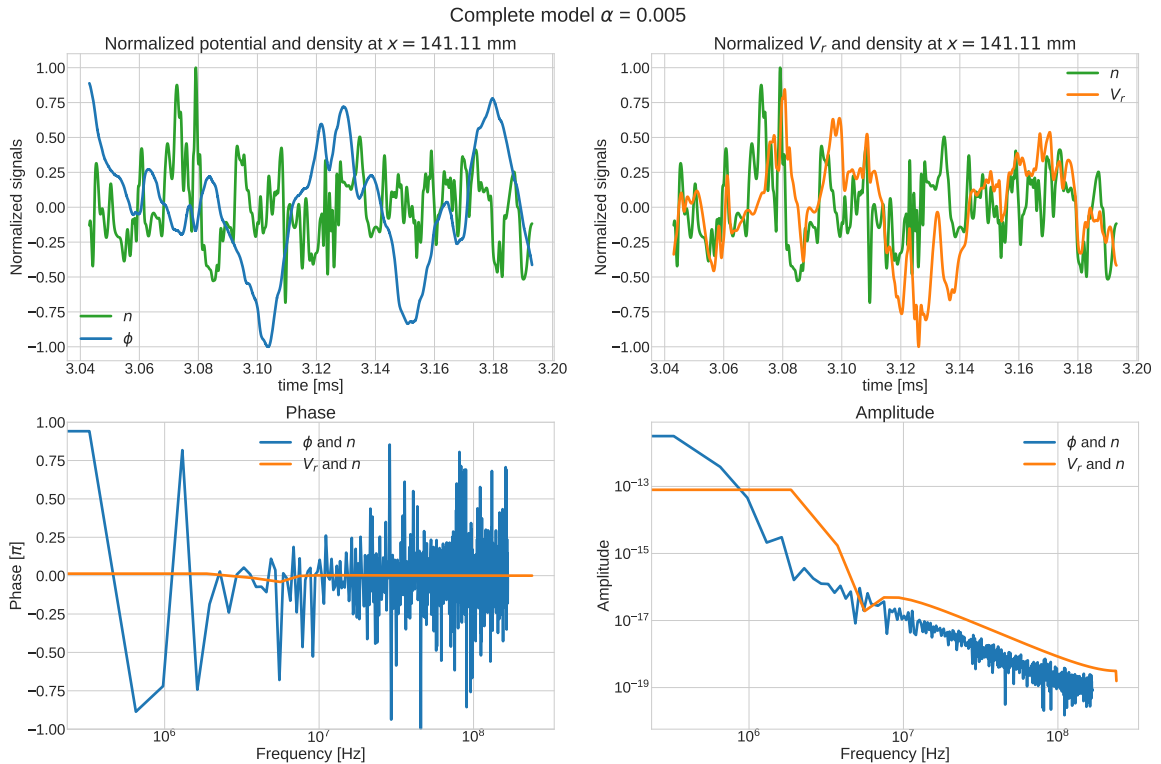

Figure 4.9: For the complete model in the scrape-off layer: normalized potential and density, top left; normalized radial velocity and density, top right; phase relation between potential and density, bottom left; and between radial velocity and density, bottom right.

In figure 4.9 it is shown that, contrary to the prediction, n and ϕ are out of phase by π rad, bottom left corner, as when the density is positive the potential is negative and vice versa, top left corner. The change from π rad to $-\pi$ rad is meaningless, as both been out of phase π rad or $-\pi$ rad is the same. This result is still not really understood and it needs further work. Also, the π rad phase for low frequencies is followed with a peak in amplitude, around 10^{-12}, that decreases quite fast, as seen in the amplitude graphic, bottom left corner. For the case of the radial velocity, we can see that both signals are not always in phase, although the general trend seems to confirm an in phase relation, top right corner. This generates a phase difference of 0 rad for all the frequencies, as seen in the phase graph, bottom left corner. This result agrees with the prediction but it is still a bit confusing, one would expect to see it clearer in the signals. when looking at the amplitude graphic, bottom right corner; we see, as in the edge, that the amplitude is highest for the lowest frequencies and maintains straight till 1.3 MHz, then it decays quite fast. This means, that similarly to the result in the edge, figure 4.8, the 0 rad phase relation is fulfilled for the v_r and n, while the relation for ϕ and n is not really fulfilled. Now it is interesting to see how does the average phase look along the radial axis.

The average phase relation between ϕ and n are depicted at the top of figure 4.10. Here we can see that in the edge region the higher α the nearer the phase is to 0 rad, the coupling becomes higher. It

is interesting to notice that near the source for $\alpha = 0.05$, there are some fluctuations, from $x = 0$ mm to $x = 26$ mm. These fluctuations might be related to the fact that in this case the turbulence is not propagated all along the full grid. As seen in figure 4.7, where the vorticity vanishes from $x = 0$ mm to $x=35$ mm, more or less for $\kappa = 0.005$. In the case of the lowest α values, 0.001 and 0.0005, we see some peaks between the end of the source, $x = 10$ mm, and the high turbulence region at, $x = 75$ mm. These peaks are related to the vorticity columns, although they seem to become smaller as α increases. At the current state of the thesis, there is no explanation, further research must be done in this area. One could suggest that it is a consequence of small turbulence created in these columns by some up and down transport. It is also important to remember that IC turbulence is also present. In the region near the interface, between $x = 75$ and 100 mm, the phase relation becomes between 0 rad and $-\frac{\pi}{4}$ rad, due to the high turbulence and it decreases to $-\frac{\pi}{2}$ rad at the LCFS, as predicted by the theory for the IC turbulence. Still, at the SOL, we can see that the phase relation goes to $\pm\pi$ for all the simulations. There is no explanation for this effect, although we can suggest that it is generated from the reflection of the potential in the boundary or from some effect from the edge. As we have already mentioned, ϕ is a global variable, which means that can be influenced from other parts of the grid. We use Neumann boundary conditions, which do not allow flux to abandon the grid and it might be reflected. Thus, we suspect that it is generated because the grid is not big enough to neglect the action range of the electric potential.
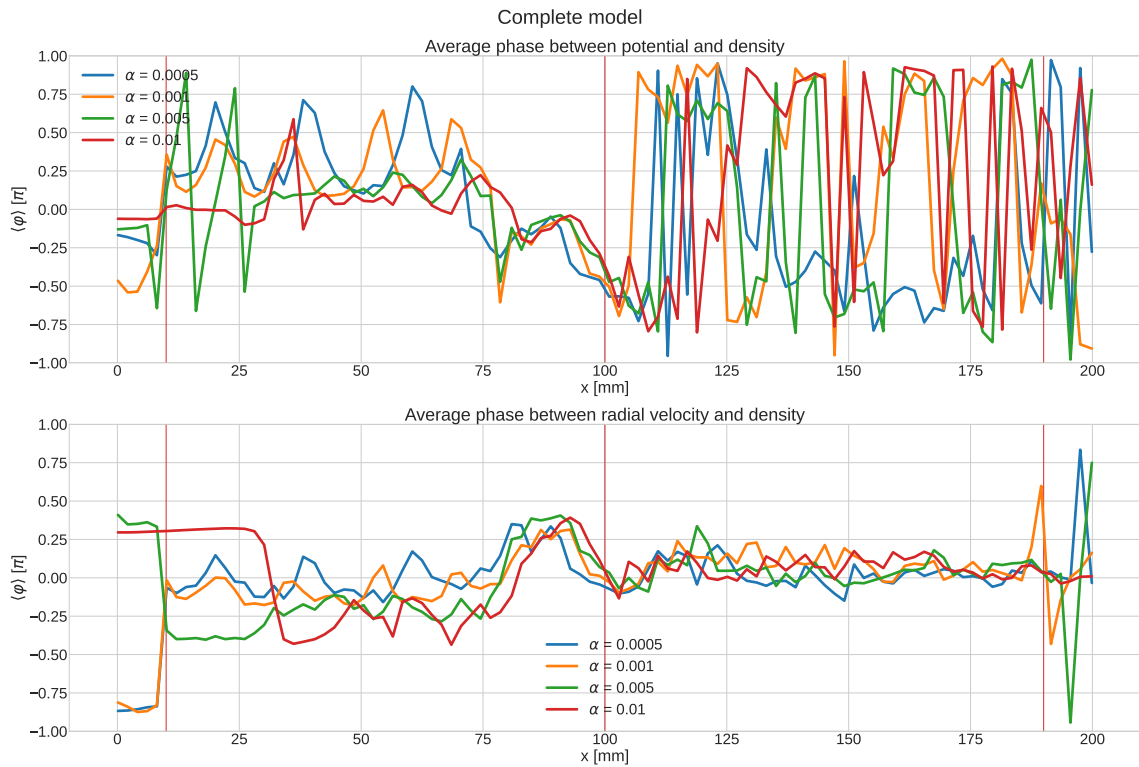

Figure 4.10: Phase relation between radial velocity and density, top; and between potential and density for the Complete model.

In the case of the radial velocity, we can see the average phase difference with respect to the density at the bottom of figure 4.10. In the inner region, we can see the same effects, more or less, higher the conductivity better the uncoupling between v_r and n, but we can see that between the source and the interface, the transport seems to be quite efficient, with almost 0 rad phase difference. The fact that the turbulence got much faster propagated with lower α give us reasons to think that the conductivity was not high enough so that DW turbulence could be dominant over the IC, we should highlight that the highest conductivity value used in this simulation is the lowest used for the HW model in the previous section. Furthermore, we shall not forget that κ is not only active at the SOL, hence IC turbulence acts in the edge. Still, we have to notice that near the LCFS, at the interface, where the turbulence seems to be more clearly produced, the phase relation gets to values between $\frac{\pi}{4}$ rad and almost $\frac{\pi}{2}$ rad and it decreases to 0 rad at the LCFS. This is an important

point, as this result suggests that from $x = 75\ mm$ until the LCFS we have a mix between DW and IC turbulence. This explains why a part from having a poloidal velocity in this range, we also have radial transport. In the SOL, we can see that we have a phase relation of nearly 0 rad all over the region, till the vorticity sink. This is a proof of the perfect transport in this region, the low amount of plasma that crosses the LCFS is directly ejected to the wall.

From both phase characterizations, it is important to mention and highlight that, although there are some questions to be answered, there seems to be a clear differentiation between the edge and the SOL at the LFCS, a part from a mix of IC and DW turbulence at the edge.

4.3 EAST experiment

Finally, we shall apply this technique to an experimental case so we can probe the validity of it in a real case. As we have already mentioned, we will use data obtained from probes inserted inside the EAST reactor. We have to highlight that this data is not ideal for our propose, as it is not detected in the same place, the prove measures while it is moving and the measurement frequency is much lower compared to the prove frequency in the simulations, $f = 1$ MHz [12] against the 13.3 GHz from the IC and HW models or 333.3 MHz with the complete model, and the way of relation between parameters makes them somehow correlated.
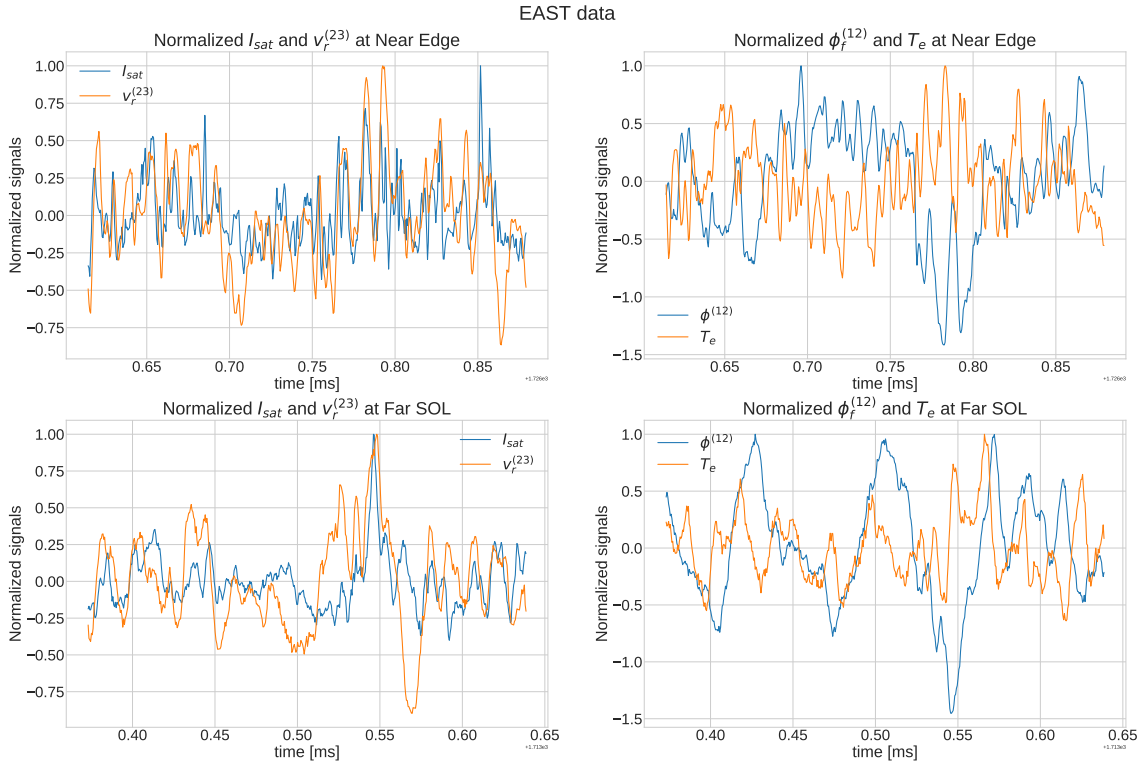

Figure 4.11: Signal comparison from the probes used in the EAST reactors. From left to right, comparison of the normalized I_{sat} and $v_r^{(23)}$ and comparison of the normalized $\phi_f^{(12)}$ and T_e. From top to bottom we have the regions of the comparison, near edge and far SOL. The signals are just a piece of the from each region, from $r = -10$ to -9.5 mm, for the near edge; and from $r = 15.5$ to 16 mm for the far SOL. The near edge signal is taking at the time range from $t = 1.726615$ to 1.726879 s and the far SOL is taking in the range from $t = 1.713373$ to 1.713639 s. Which is a bit unclear in graphs.

The first thing we need to do is to decide which variables use, as there are more than 10 possible variables, from section 2.3. One could argue that the best would be to apply the CPSD to compare the density with the plasma potential, which is optimal as they are measured at different poloidal position and they are related through the temperature, equations 2.88 and 2.89. Hence, the next obvious couple of variables are the density and the radial velocity. We can approximate the density as ion saturation, so that $n \approx I_{sat}$, which allows us to not rely on T_e and calculate the radial velocity

at the same poloidal position, as $v_r^{(23)}$ using equation 2.90. Also, we propose to use T_e and the floating potential $\phi_f^{(12)}$, calculated with equation 2.86. T_e and $\phi_f^{(12)}$ are linearly dependant through equations 2.87 and 2.88, but they are the only couple of variables giving a reasonable solution, as we will see.

In figure 4.11 we have plotted I_{sat} and $v_r^{(23)}$ versus time, in the left side; and $\phi_f^{(12)}$ and T_e versus time, in the right side. We have separated the plots in 2 regions, the near edge, at the top; and the far SOL, at the bottom. We should expect to see similar graphs for the far edge and near SOL. The time regions at the near edge are from $t = 1.726615$ to 1.726879 s, corresponding to $r = -10$ to -9.5 mm; and at the far SOL from $t = 1.713373$ to 1.713639 s, corresponding to $r = 15.5$ to 16 mm. When comparing I_{sat} anf $v_r^{(23)}$ at the near edge, top left corner, we can see that, even if there are some places that the frequency of each signal is not the same or there are a bit out of phase, the general trend indicates that I_{sat} and $v_r^{(23)}$ are in phase along the whole near edge. At the far SOL, we have the same result, although the frequency of $v_r^{(23)}$ is much lower, when $v_r^{(23)}$ is maximum, also is I_{sat} and the other way around, when $v_r^{(23)}$ is minimum, also I_{sat} is minimum. Hence, we might not find a way of distinguishing the SOL from the edge using these signals together. When looking at the $\phi_f^{(12)}$ and T_e signals at the near edge, top right corner, we can see that whenever one is maximum the other is minimum, which makes sense as T_e depends linearly on $-\phi^{(12)}$, equation 2.87. Therefore, at the edge we should expect a $\pm\pi$ rad phase difference. When looking at the SOL, bottom left corner, we can see the same tendency, but some of the peaks are shifted, as T_e also depends on ϕ^+. This local variations in the phase, will give us a phase relation different from $\pm\pi$, which is our aim to be able of measuring the LCFS using this technique.
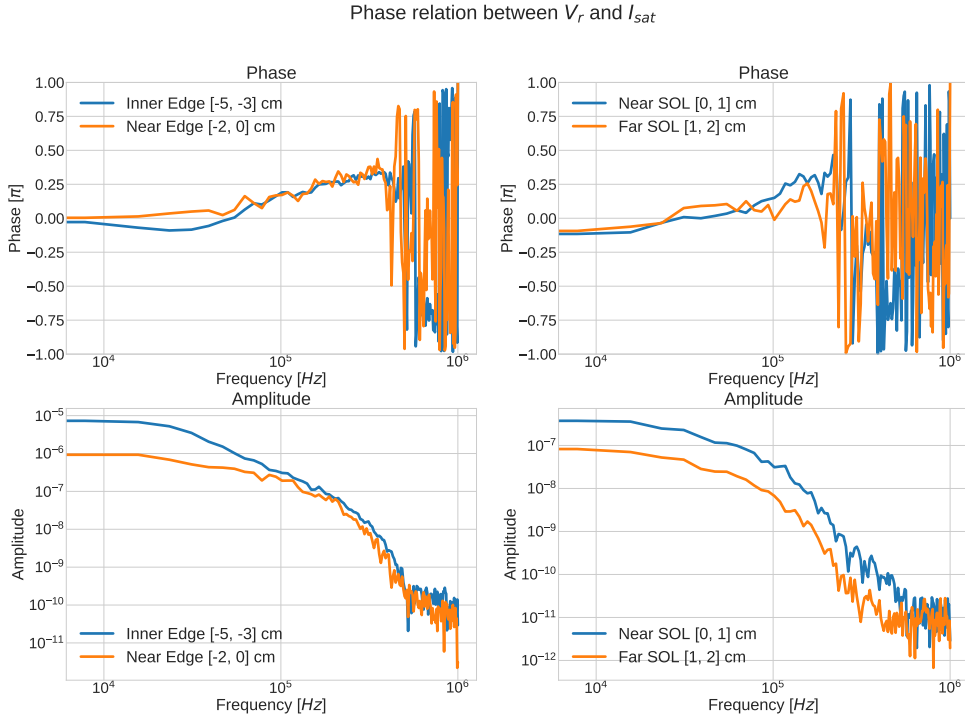

Figure 4.12: CPSD between radial velocity and ion saturation. Phase relation in the top and amplitude, or contribution, in the bottom. Edge region in the left and SOL in the right.

The phase relation between I_{sat} and $v_r^{(23)}$ can be seen in figure 4.12. Here we can see that the amplitude, depicted at the bottom of the figure, does not decay so fast as we have seen from the simulations, basically because the lowest frequencies are the ones with higher contribution and the frequencies that we study here are much lower. Still, from 0 to $f = 10^5$ Hz we can accept to have the most important ones, as the amplitude decays 1 order of magnitude in that range. In this range, we can see that the phase difference, depicted at the top of the image, is almost 0 rad at all the parts of the reactor, although it is a bit lower at the SOL, around $-\frac{\pi}{10}$ rad, instead of 0 rad as in the edge. This relation makes it really hard to actually distinguish both regions.
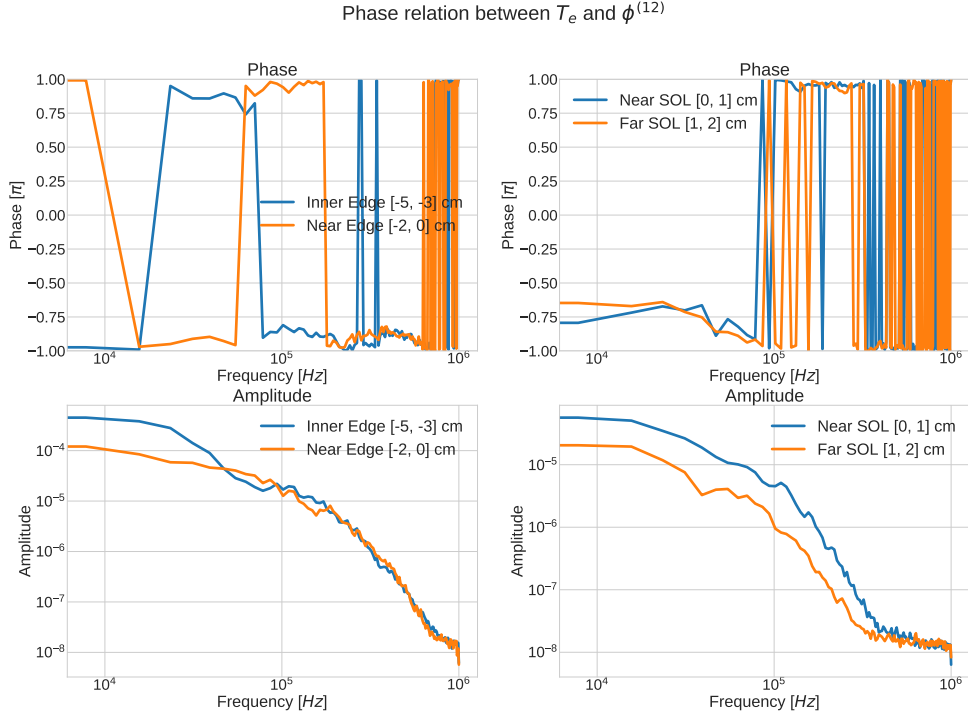
Figure 4.13: CPSD between the electron temperature and the floating potential $\phi_f^{(12)}$. Phase relation in the top and amplitude, or contribution, in the bottom. Edge region in the left and SOL in the right.

The phase relation between $\phi_f^{(12)}$ and T_e can be seen in figure 4.13. Here we can see that the amplitude, depicted at the bottom of the figure, decays more or less as it does for the other pair of variables, as seen at the bottom of figure 4.12. Having the peak at the beginning and decaying 1 order of magnitude by $f = 10^5$ Hz. Looking again at the phases in these frequencies, we see that in the edge, the phases rotate between π rad and $-\pi$ rad, as we already predict, which is equivalent. Hence, at the edge, the phase shift is π rad. When we look at the SOL, this is not the case, the phase relations are almost $-\frac{3\pi}{4}$ rad, higher the nearer we are to the LCFS, -0.6π rad in the near SOL. Therefore, when looking at this pair of variables, we can characterize and separate these two regions, giving an idea of the position of the LCFS.

Chapter 5

Conclusions

From the experiments that have been performed during this project, we can get some conclusions and propose further improvements for a better understanding and more accurate solution from the simulations.

From the interchange model, we can see that the use of Dirichlet boundary conditions generates equipartition turbulence. Which means that the linearization of the model using plane waves to study the phase between variables, section 2.2.4, is not completely satisfactory. The big vortexes control the transport and synchronize the potential with the density. However, in this regime, the radial velocity and the density continue been in phase, the transport is perfect. For further studies of this model, we suggest to reduce the Reynolds number, if we increase the viscosity or change the size of the grid, we should be able of erasing this equipartition state [41]. Furthermore, one could use Neumann boundary conditions at $x = l_x$ and add a source in the left boundary, same as we did for the complete model. This would allow the plasma to escape the system while maintaining the system stable. Therefore, the equipartition turbulence would not be created, allowing the study the phase difference between ϕ and n without having to place the probes between the vortexes.

For the modified Hasegawa-Wakatani model, we can conclude that the obtained solution is satisfactory. It fulfills the theoretical prediction, we found that ϕ and n evolve in phase, while v_r and n evolve out of phase, even if the difference is not strictly $\pm \frac{\pi}{2}$ rad. For further studies, the contribution of zonal modes to the phase shift between radial transport and density could be investigated.

The complete model still needs to be studied in more detail, more simulations must be done. Most of the simulations did not achieved a completely propagated turbulent state and the coupling between ϕ and n might be influenced by the magnetic curvature. Higher values of α should be tried, or lower of κ. For the modified HW model, alone, we used values from 0.0125 to 0.2, where only $\alpha = 0.2$ got the expected $\frac{\pi}{2}$ rad phase relation between v_r and n, synchronized with the zonal modes. While, for the complete model we used values from 0.0005 to 0.01, lower than the lowest used for the HW model. Hence, increasing the evolution time as well as the conductivity, should help us to understand were do the anomalies come from in the edge. If the peaks shown in figure 4.10 come from the zonal modes, from the interchange dynamics or if there is any other process. In this regard, we have to mention that G. Decristoforo et al [20] let the equations evolve for $2 \cdot 10^6$ time units. In the process of this work, it was not possible to try this, as the limited time of simulation in the Marconi100 cluster, 24h maximum, and the low stability of the simulations needed of further research and changes in the code so we could experiment with larger periods. Therefore, we needed a way of ensuring a stable simulation with higher α and a way of achieving a quasi stable state, where the instability is completely propagated along the grid, regardless the time limitation of the simulation. This could be possible by saving the grid and using it as initial condition every time the simulation ends. However, the solution is still satisfactory, we can be positive, as there seems to be good reason to believe that the phase relation could be used to calculate the position of the LCFS, as in figure 4.10 we can see that there is a change in the phase at both sides of the LCFS; and the phase relation at the end of the edge suggest an interesting regime where both instabilities are present. Furthermore, the obtained phase relation could be used to study how dominant is one instability over the other and their relation with α and κ.

Regarding the data from EAST, if we want to calculate the LCFS inside a nuclear fusion reactor with this method, we need further research. The diagnosis technique used to get the data is not ideal, it is hard to find measures in the same poloidal position that are not correlated between themselves

and can give a satisfactory phase relation. Furthermore, we could find an interesting solution for the floating potential at the poloidal position as the biased probe, $\phi_f^{(12)}$, compared to the electron temperature. Variables that depend on each other. The rest of the variables that were tried did not show any change in the phase difference between the edge and the scrape-off layer. Hence, we need a measurement method that matches better our simulations, maybe by steady measurements, our data was measured in movement, and probably at higher frequency. As we can see from figures 4.2, 4.5, 4.8 and 4.8, reducing the measurement frequency, in our simulations, for the cross-power spectral density could affect our results. If one wants to try this in our simulations, one should keep one point every a thousand. However, this should be studied. Nonetheless, the use of $\phi_f^{(12)}$ and T_e is quite satisfactory and indicates that we could actually use the CPSD to characterize the turbulence inside a tokamak and measure the LCFS, which could reduce significantly the costs of this process.

In the future, we need to make our simulations and our experimental data more comparable. For that reason, we should escalate this model to a 3D model and increase the complexity of it, adding more variables. Even though, the results of the simulations speak for themselves, they do not really match the experimental values. The only parameters from which we could find a suitable characterization, for EAST, are T_e and $\phi_f^{(12)}$. Values that are not calculated in our simulations.

As a final remark, even if there is still space for improvement and there are open questions. We have demonstrated the viability of the phase relation as a method to characterize turbulence and study the regions around the LCFS through our simulations. This could have an important role in the future of nuclear fusion energy, plasma dynamics and the study of turbulent states.

Bibliography

[1]   A. Welch, "Pollution linked to 9 million deaths worldwide each year," *CBS News*, Oct. 2017. [Online]. Available: https://www.cbsnews.com/news/pollution-9-million-deaths-worldwide-each-year/.

[2]   M. Pehl, A. Arvesen, F. Humpenöder, A. Popp, E. G. Hertwich, and G. Luderer, "Understanding future emissions from low-carbon power systems by integration of life-cycle assessment and integrated energy modelling," *Nature Energy*, vol. 2, no. 12, pp. 939–945, Dec. 2017, ISSN: 2058-7546. DOI: 10.1038/s41560-017-0032-9. [Online]. Available: https://doi.org/10.1038/s41560-017-0032-9.

[3]   B. Looney, "Statistical review of world energy," *bq*, 2020. [Online]. Available: https://www.bp.com/en/global/corporate/energy-economics/statistical-review-of-world-energy.html.

[4]   N. Seko, A. Katakai, S. Hasegawa, M. Tamada, N. Kasai, H. Takeda, T. Sugo, and K. Saito, "Aquaculture of uranium in seawater by a fabric-adsorbent submerged system," *Nuclear Technology*, vol. 144, no. 2, pp. 274–278, 2003. DOI: 10.13182/NT03-2. eprint: https://doi.org/10.13182/NT03-2. [Online]. Available: https://doi.org/10.13182/NT03-2.

[5]   J. P. Freidberg, *Plasma Physics and Fusion Energy*. Cambridge University Press, 2007. DOI: 10.1017/CBO9780511755705.

[6]   D. A. Shea and D. Morgan, "The helium-3 shortage: Supply, demand, and options for congress," *Congressional Research Service*, 2010.

[7]   "Helium-3 mining on the lunar surface," *ESA (The European Space Agency)*, [Online]. Available: https://www.esa.int/Enabling_Support/Preparing_for_the_Future/Space_for_Earth/Energy/Helium-3_mining_on_the_lunar_surface.

[8]   P. S. Garry M. McCracken, *Fusion: The Energy of the Universe*, 1st ed., ser. Complementary Science. Academic Press, 2005, ISBN: 0123846560.

[9]   Y. Xu, "A general comparison between tokamak and stellarator plasmas," *Matter and Radiation at Extremes*, vol. 1, no. 4, pp. 192–200, Jul. 2016. DOI: 10.1016/j.mre.2016.07.001. [Online]. Available: https://doi.org/10.1016/j.mre.2016.07.001.

[10] *ITER (International Thermonuclear Experimental Reactor)*. [Online]. Available: http://iter.org/.

[11] *EAST (the Experimental Advanced Superconducting Tokamak)*. [Online]. Available: http://english.ipp.cas.cn/.

[12] N. Yan, A. H. Nielsen, G. S. Xu, V. Naulin, J. J. Rasmussen, J. Madsen, H. Q. Wang, S. C. Liu, W. Zhang, L. Wang, and B. N. Wan, "Statistical characterization of turbulence in the boundary plasma of EAST," vol. 55, no. 11, p. 115 007, Oct. 2013. DOI: 10.1088/0741-3335/55/11/115007. [Online]. Available: https://doi.org/10.1088/0741-3335/55/11/115007.

[13] A. N. Simakov and P. J. Catto, "Drift-ordered fluid equations for field-aligned modes in low-β collisional plasma with equilibrium pressure pedestals," *Physics of Plasmas*, vol. 10, no. 12, pp. 4744–4757, Dec. 2003. DOI: 10.1063/1.1623492. [Online]. Available: https://doi.org/10.1063/1.1623492.

[14] F. F. Chen, *Introduction to Plasma Physics and Controlled Fusion*. Springer, 2016. DOI: 10.1017/CBO9780511807183.

[15] O. E. García, "Collective motions in non-uniformly magnetized plasmas," *European journal of physics*, vol. 24, no. 4, pp. 331–339, 2016. DOI: 10.1088/0143-0807/24/4/351.

[16] P. M. Bellan, *Cambridge University Press*. Springer, 2004. DOI: 10.1007/978-3-319-22309-4.

[17] R. Kube, O. E. García, and M. Wiesenberger, "Amplitude and size scaling for interchange motions of plasma filaments," *Physics of Plasmas*, vol. 23, no. 12, p. 122 302, 2016. DOI: 10.1063/1.4971220.

[18] S. B. Korsholm, "Coherent structures and transport in drift wave plasma turbulence," Ph.D. dissertation, Danmarks Tekniske Universitet (DTU), 2011.

[19] J. Anderson and B. Hnat, "Statistical analysis of hasegawa-wakatani turbulence," *Physics of Plasmas*, vol. 24, p. 062 301, 2017. DOI: 10.1063/1.4984985.

[20] G. Decristoforo, A. Theodorsen, J. Omotani, T. Nicholas, and O. E. Garcia, "Numerical turbulence simulations of intermittent fluctuations in the scrape-off layer of magnetized plasmas," 2021. arXiv: 2102.04723 [physics.plasm-ph].

[21] N. Yan, "Coherent structures in the boundary plasma of east tokamak," Ph.D. dissertation, Danmarks Tekniske Universitet (DTU), 2014.

[22] J. Madsen, V. Naulin, A. H. Nielsen, and J. J. Rasmussen, "Collisional transport across the magnetic field in drift-fluid models," *Physics of Plasmas*, vol. 23, no. 3, Mar. 2016, ISSN: 1070-664X. DOI: 10.1063/1.4943199. [Online]. Available: https://www.osti.gov/biblio/22599038.

[23] P. D. Ditlevsen, *Turbulence and Shell Models*. Cambridge University Press, 2010. DOI: 10.1017/CBO9780511919251.

[24] M. Wiesenberger, *Various advection schemes*, https://mwiesenberger.github.io/advection/comparison.html#order-1-artificial-viscosity, 2020.

[25] A. Hasegawa and M. Wakatani, "Plasma edge turbulence," *Phys. Rev. Lett.*, vol. 50, pp. 682–686, 9 1983. DOI: 10.1103/PhysRevLett.50.682. [Online]. Available: https://link.aps.org/doi/10.1103/PhysRevLett.50.682.

[26] A. Kendl, "On radial geodesic forcing of zonal modes," *Physics of Plasmas*, vol. 18, no. 7, p. 072 303, Jul. 2011. DOI: 10.1063/1.3603838. [Online]. Available: https://doi.org/10.1063/1.3603838.

[27] P. Stangeby, *The Plasma Boundary of Magnetic Fusion Devices*. CRC Press, 2000. DOI: https://doi.org/10.1201/9780367801489.

[28] M. Wiesenberger and M. Held, *FELTOR (Full-F ELectromagnetic code in TORoidal geometry)*. DOI: https://doi.org/10.5281/zenodo.1290270. [Online]. Available: https://feltor-dev.github.io/.

[29] J. S. Hesthaven and T. Warburton, *Nodal Discontinuous Galerkin Methods, Algorithms, Analysis, and Applications*. Springer, 2008. DOI: https://doi.org/10.1007/978-0-387-72067-8.

[30] C. Rodríguez and M. Wiesenberger, *Feltor 2d master thesis*, 2021. [Online]. Available: https://github.com/PPFE-Turbulence/Feltor_2D_Master_Thesis.git.

[31] M. Wiesenberger, "Gyrofluid computations of filament dynamics in tokamak scrape-off layers," Ph.D. dissertation, University of Innsbruck, 2014.

[32] F. Celiker and B. Cockburn, "Superconvergence of the numerical traces of discontinuous galerkin and hybridized mixed methods for convection-diffusion problems in one space dimension," *Math. Comp*, pp. 67–96, 2006.

[33] R. Courant, K. Friedrichs, and H. Lewy, "On the partial difference equations of mathematical physics," *IBM Journal of Research and Development*, vol. 11, no. 2, pp. 215–234, 1967. DOI: 10.1147/rd.112.0215.

[34] G. E. Karniadakis, M. Israeli, and S. A. Orszag, "High-order splitting methods for the incompressible navier-stokes equations," *Journal of Computational Physics*, vol. 97, no. 2, pp. 414–443, 1991, ISSN: 0021-9991. DOI: https://doi.org/10.1016/0021-9991(91)90007-8. [Online]. Available: https://www.sciencedirect.com/science/article/pii/0021999191900078.

[35] S. J. Ruuth and W. Hundsdorfer, "High-order linear multistep methods with general monotonicity and boundedness properties," *Journal of Computational Physics*, vol. 209, no. 1, pp. 226–248, 2005, ISSN: 0021-9991. DOI: https://doi.org/10.1016/j.jcp.2005.02.029. [Online]. Available: https://www.sciencedirect.com/science/article/pii/S0021999105000951.

[36] P. Bogacki and L. Shampine, "A 3(2) pair of runge - kutta formulas," *Applied Mathematics Letters*, vol. 2, no. 4, pp. 321–325, 1989, ISSN: 0893-9659. DOI: https://doi.org/10.1016/0893-9659(89)90079-7. [Online]. Available: https://www.sciencedirect.com/science/article/pii/0893965989900797.

[37] S. V. Patankar, *Numerical Heat Transfer and Fluid Flow*. Taylor & Francis, 1980. DOI: https://doi.org/10.1201/9781482234213. [Online]. Available: https://www.taylorfrancis.com/books/mono/10.1201/9781482234213/numerical-heat-transfer-fluid-flow-suhas-patankar.

[38] W. D. Penny, *Signal processing course, chapter 7*, 2009. [Online]. Available: https://www.fil.ion.ucl.ac.uk/~wpenny/course/course.html.

[39] P. Welch, "The use of fast fourier transform for the estimation of power spectra: A method based on time averaging over short, modified periodograms," *IEEE Transactions on Audio and Electroacoustics*, vol. 15, no. 2, pp. 70–73, 1967. DOI: 10.1109/TAU.1967.1161901.

[40] P. Virtanen, R. Gommers, T. E. Oliphant, M. Haberland, T. Reddy, D. Cournapeau, E. Burovski, P. Peterson, W. Weckesser, J. Bright, S. J. van der Walt, M. Brett, J. Wilson, K. J. Millman, N. Mayorov, A. R. J. Nelson, E. Jones, R. Kern, E. Larson, C. J. Carey, İ. Polat, Y. Feng, E. W. Moore, J. VanderPlas, D. Laxalde, J. Perktold, R. Cimrman, I. Henriksen, E. A. Quintero, C. R. Harris, A. M. Archibald, A. H. Ribeiro, F. Pedregosa, P. van Mulbregt, and SciPy 1.0 Contributors, "SciPy 1.0: Fundamental Algorithms for Scientific Computing in Python," *Nature Methods*, vol. 17, pp. 261–272, 2020. DOI: 10.1038/s41592-019-0686-2.

[41] V. Naulin, J. Juul Rasmussen, and J. Nycander, "Transport barriers and edge localized modes-like bursts in a plasma model with turbulent equipartition profiles (erratum in phys. plasmas v. 9, 3804 (2003))," English, *Physics of Plasmas*, vol. 10, no. 4, pp. 1075–1082, 2003, ISSN: 1070-664X. DOI: 10.1063/1.1559993.

[42] O. E. Garcia, N. H. Bian, V. Naulin, A. H. Nielsen, and J. J. Rasmussen, "Two-dimensional convection and interchange motions in fluids and magnetized plasmas," *Physica Scripta*, vol. T122, pp. 104–124, Jan. 2006. DOI: 10.1088/0031-8949/2006/t122/014. [Online]. Available: https://doi.org/10.1088/0031-8949/2006/t122/014.

[43] A. Nielsen, O. Asztalos, J. Olsen, V. Naulin, J. J. Rasmussen, A. Thrysøe, T. Eich, G. Pokol, N. Vianello, R. Coelho, D. Refy, B. Tal, A. Buzas, G. Hu, and N. Yan, "Synthetic edge and scrape-off layer diagnostics-a bridge between experiments and theory," *Nuclear Fusion*, vol. 59, no. 8, p. 086 059, Jul. 2019. DOI: 10.1088/1741-4326/ab1954. [Online]. Available: https://doi.org/10.1088/1741-4326/ab1954.